Traffic 2011; 12: 452–472

doi:10.1111/j.1600-0854.2011.01160.x

Hydrophobic-Domain-Dependent Protein–Protein Interactions Mediate the Localization of GPAT Enzymes to ER Subdomains

Satinder K. Gidda[1], Jay M. Shockey[2], Mina Falcone[3], Peter K. Kim[4], Steven J. Rothstein[1], David W. Andrews[3], John M. Dyer[5,*] and Robert T. Mullen[1,*]

[1]Department of Molecular and Cellular Biology, University of Guelph, Guelph, ON, Canada
[2]USDA-ARS, Southern Regional Research Center, New Orleans, LA, USA
[3]Department of Biochemistry and Biomedical Sciences, McMaster University, Hamilton, ON, Canada
[4]Cell Biology Program, The Hospital for Sick Children, Toronto, ON, Canada
[5]USDA-ARS, US Arid-Land Agricultural Research Center, Maricopa, AZ, USA
**Corresponding author: Robert T. Mullen, rtmullen@uoguelph.ca; John M. Dyer, John.Dyer@ars.usda.gov*

The endoplasmic reticulum (ER) is a dynamic organelle that consists of numerous regions or 'subdomains' that have discrete morphological features and functional properties. Although it is generally accepted that these subdomains differ in their protein and perhaps lipid compositions, a clear understanding of how they are assembled and maintained has not been well established. We previously demonstrated that two diacylglycerol acyltransferase enzymes (DGAT1 and DGAT2) from tung tree (*Vernicia fordii*) were located in different subdomains of ER, but the mechanisms responsible for protein targeting to these subdomains were not elucidated. Here we extend these studies by describing two glycerol-3-phosphate acyltransferase-like (GPAT) enzymes from tung tree, GPAT8 and GPAT9, that both colocalize with DGAT2 in the same ER subdomains. Measurement of protein–protein interactions using the split-ubiquitin assay revealed that GPAT8 interacts with itself, GPAT9 and DGAT2, but not with DGAT1. Furthermore, mutational analysis of GPAT8 revealed that the protein's first predicted hydrophobic region, which contains an amphipathic helix-like motif, is required for interaction with DGAT2 and for DGAT2-dependent colocalization in ER subdomains. Taken together, these results suggest that the regulation and organization of ER subdomains is mediated at least in part by higher-ordered, hydrophobic-domain-dependent homo- and hetero-oligomeric protein–protein interactions.

Key words: diacylglycerol acyltransferase, endoplasmic reticulum, glycerol-3-phosphate acyltransferase, protein–protein interactions, protein targeting, protein topology, subdomain

Received 20 September 2010, revised and accepted for publication 6 January 2011, uncorrected manuscript published online 7 January 2011, published online 8 February 2011

A hallmark of eukaryotic cells is the compartmentalization of proteins into distinct membrane-bound organelles. This 'division of labor' allows for specialized sets of enzymes to operate in a cooperative manner and thereby ensuring the specificity and fidelity of the metabolic pathways that are essential to the overall functionality of the cell. Functional compartmentalization also exists within individual organelles and often involves specific collections of proteins and other membrane-embedded components. That is, many (if not all) organelle membranes contain discrete, short-range ordered structures or 'subdomains' that, compared to the surrounding membrane, carry out unique functions (1). For instance, the membrane electron transport chains within mitochondria and chloroplasts consist of a number of proteins that are organized as relatively stable supercomplexes (2,3). Other organelle subdomains such as plastid stromules, peroxisomal peroxules and mitochondrial matrixules are highly dynamic, transient structures that project from the surface of these organelles and occasionally form intra- and inter-organelle connections (4–6).

Perhaps the most striking example of subdomain organization is in the endoplasmic reticulum (ER), a continuous, but pleomorphic network of membrane tubules and sheet-like cisternae that has long been recognized to contain several functionally distinct regions (7–12). For instance, rough ER is a subdomain of the ER studded with membrane-bound ribosomes and as such is involved in co-translational protein synthesis and import into the organelle. Smooth ER, on the other hand, is an ER subdomain that lacks ribosomes, but serves as a reservoir of Ca^{2+} and is enriched in enzymes associated with a variety of metabolic pathways including lipid and steroid biosynthesis, carbohydrate metabolism and drug detoxification. Other notable ER subdomains include transitional ER or so-called ER export sites, wherein newly synthesized secretory proteins exit via coatomer protein II (COPII) coated vesicles (13,14), peroxisomal ER (15), which is involved in the trafficking of a subset of membrane-bound proteins to peroxisomes, and prolamine- and glutelin-enriched regions of the ER, which are involved in the production and deposition of storage proteins into protein bodies within the developing seeds of some plants (16).

The ER also plays a central role in the production of lipids in eukaryotic cells and a number of discrete subdomains have been identified that are associated with this activity. For instance, the biosynthesis of storage triacylglycerols (TAGs) occurs in the ER. This is a complex process whereby nascent TAGs accumulate at certain regions within the ER lipid bilayer and then,

under some unknown influence, bud off to form a lipid droplet or 'oil body' (17–19). In mammalian cells, freeze fracture immuno-electron microscopy (20) and live-cell video microscopy (21,22) have shown that proteins involved in oil body biosynthesis are enriched in distinct regions of the ER membrane. Similarly, in plant cells, the enzyme diacylglycerol acyltransferase (DGAT), which catalyzes the committed step in TAG production, is localized in distinct regions of ER (23). Interestingly, plant cells contain two unrelated types of DGAT proteins (i.e. DGAT1 and DGAT2) that are each capable of synthesizing TAG, but have different substrate/product relationships and are located in different subdomains of ER (23).

Although the molecular mechanisms underlying the spatiotemporal formation and maintenance of organelle subdomains are not well understood, there is a growing consensus that they are governed largely by the principles of self-assembly via specific protein–protein (either homotypic and/or heterotypic) and/or protein–lipid interactions (7,13,24,25). Thus, gaining a better understanding of subdomain biogenesis is important not only for understanding the overall architecture of eukaryotic cells and organelles, but also for the fundamental processes of macromolecular interactions and intracellular membrane trafficking. Previously, we demonstrated that DGAT1 and DGAT2 of the tung tree (*Vernicia fordii*) are localized in different, dynamic subdomains of the ER when expressed in tobacco cells (23). Here we describe the identification of two glycerol-3-phosphate acyltransferase (GPAT) enzymes (GPAT8 and GPAT9) from tung tree that colocalize in the subdomains of ER, and interestingly, they also colocalize with DGAT2, but not with DGAT1. Investigation of protein–protein interactions using the split-ubiquitin (split-Ub) membrane yeast two-hybrid assay revealed that GPAT8 interacted with itself, GPAT9 and DGAT2, but not with DGAT1. Furthermore, by using site-directed mutagenesis and a combination of *in vivo* protein trafficking experiments and complementary protein–protein interaction analyses via split-Ub, we also demonstrate that the first predicted hydrophobic region of GPAT8, which contains an amphipathic helix-like motif known to modulate interactions and assembly of other membrane proteins (26–28), serves as a critical element for mediating ER subdomain localization. The implications of these results in terms of ER subdomain biogenesis via higher-ordered protein homo- and heterotypic interactions as well as protein–lipid interactions are discussed.

Results

Identification of GPAT8 and GPAT9 genes from tung tree

As part of our ongoing effort to characterize the acyltransferases involved in lipid metabolism in plants (23,29,30), we identified a GPAT-like coding sequence in an expressed sequence tag (EST) library derived from the tung tree. Tung is a subtropical tree that produces seed

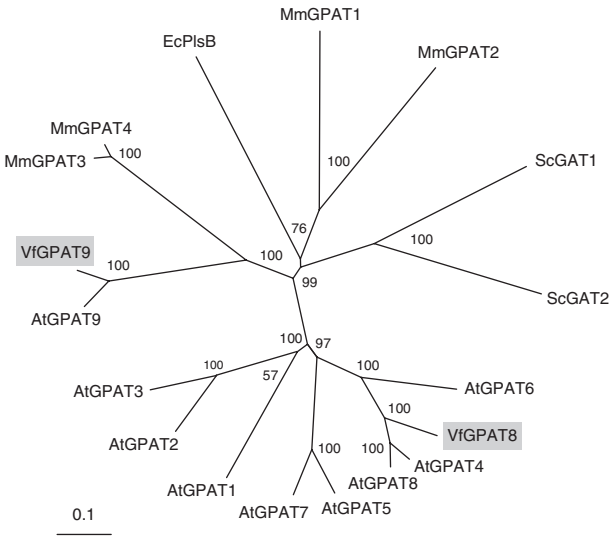

Figure 1: Phylogenetic analysis of GPAT proteins from diverse organisms. Neighbor-joining tree based on the degree of sequence similarity between GPAT sequences from *Arabidopsis thaliana* (At), *Saccharomyces cerevisiae* (Sc), *Escherichia coli* (Ec), tung tree (Vf) (shaded gray) and *Mus musculus* (Mm) (see *Materials and Methods* for database accession numbers and specific details of protein names). The branch lengths of the tree are proportional to divergence and the 0.1 scale indicates 0.1 substitutions per site. Bootstrap values are shown in percentages at the nodes of the tree.

oil enriched in α-eleostearic acid (9^{cis}, 11^{trans}, 13^{trans}-octadecatrienoic acid), an unusual conjugated fatty acid that imparts industrially important drying qualities to tung oil. Recovery of the full-length coding sequence derived from the EST (see *Materials and Methods* for details) revealed that the tung GPAT sequence was most similar to GPAT8 of *Arabidopsis* (Figure 1). There are nine GPAT-like genes in *Arabidopsis*, with GPAT1–GPAT8 sharing significant sequence similarity (Figure 1). The GPAT enzymes, in general, catalyze the first step of glycerolipid biosynthesis in plants by transferring a fatty acyl group from the acyl-CoA pool to glycerol-3-phosphate to produce a lysophosphatidic acid (31). GPAT1 was previously shown to be important for pollen development (32), whereas GPAT4, 5 and 8 are involved in cuticular lipid biosynthesis (33–35). GPAT9 has not yet been functionally characterized in plants, but shows the greatest sequence similarity with GPAT3 from mammalian cells (Figure 1), which is involved in the synthesis of storage TAGs (36). Thus, given the potential importance of GPAT9 in storage oil synthesis in plants, we also cloned a GPAT9-like gene from tung tree (see *Materials and Methods*).

Alignments of GPAT8- and GPAT9-like proteins from various plant species revealed a high degree of overall amino acid sequence similarity and length within each family, including the presence of several conserved amino acids in the C-terminal half of the protein that are known to be important for substrate binding and acyltransferase

activity (Figures S1 and S2). The proteins also contained several hydrophobic regions of various lengths in their N-terminal halves and, as reported previously (30), also possessed either conserved or divergent dilysine or hydrophobic pentapeptide ER retrieval motifs at their C-termini (Figures S1 and S2). Taken together, these observations support a role for these enzymes in catalyzing GPAT activity in the ER of plant cells.

Tung GPAT8 and GPAT9 are localized to the same ER subdomains

To begin to investigate the subcellular properties of tung GPAT8 and GPAT9 proteins, the proteins were transiently expressed in tobacco Bright Yellow-2 (BY-2) suspension-cultured cells, which serve as a well-characterized model plant cell system for studying protein targeting and biogenesis (37,38). Specifically, cDNAs encoding epitope- or fluorescent protein-tagged versions of each GPAT protein were biolistically bombarded into BY-2 cells and then the fluorescence patterns attributable to the ectopically expressed proteins were examined by immuno- or auto-fluorescence confocal laser-scanning microscopy (CLSM) and compared to the (immuno)fluorescence pattern attributable to endogenous or co-expressed organellar markers.

As shown in the representative low-magnification images in Figure 2A, both N-terminal Myc-epitope-tagged GPAT8 (top row) and GPAT9 (bottom row) exhibited immunofluorescence patterns in medial (mid-cell) optical sections of formaldehyde-fixed BY-2 cells that colocalized generally with the fluorescence pattern of fluor-conjugated concanavalin-A (Con A), a commonly used marker stain for the ER (39). That is, both Myc-GPAT8 and Myc-GPAT9 localized throughout the entire Con A-stained ER network, which, when viewed at the medial region of a BY-2 cell (as in Figure 2A), includes tubules and sheet-like cisterna in the perinuclear and transvacuolar regions, as well as near the cell periphery (40). When these same cells were examined at higher magnification, however, portions of the staining patterns attributable to Myc-GPAT8 or Myc-GPAT9 appeared more punctate in nature, such that the protein fluorescence was enriched in certain regions of Con A-stained ER (positions marked by solid arrowheads) and absent in other regions (open arrowheads) (Figure 2A).

To rule out that this (punctate) staining pattern was a result of aqueous chemical fixation (e.g. partial collapse of the ER network), we also investigated GPAT protein localization in living cells using the green fluorescent protein (GFP). As shown in Figure S3A, expression of GFP-GPAT8 or GFP-GPAT9 revealed similar distinct punctate fluorescent structures that were associated with co-expressed RFP-ER (a red fluorescent protein marker of the ER lumen (23,40)). Notably, these types of punctate structures were not observed when GFP-Cb5, a cytochrome b_5 (GFP) fusion protein known to be localized generally throughout the entire ER (23,41), was co-expressed with RFP-ER in living or formaldehyde-fixed BY-2 cells (Figure S3B). As an additional control, we investigated the subcellular localization of transiently expressed GFP-Sec24, a soluble fusion protein known to associate with a well-characterized ER membrane subdomain, i.e. ER export sites for COPII vesicle budding (42). Examination of GFP-Sec24 localization in either fixed or living cells (Figure S3C) revealed similar cytosolic and ER subdomain localization patterns, despite a modest change in ER morphology because of the formaldehyde fixation, as expected (43–46). Taken together, these results indicate that the GPAT8 and GPAT9 proteins are enriched in distinct regions of ER and that this localization pattern is not simply an artifact because of chemical fixation.

To further examine the relationship of the GPAT subdomains to the ER network overall, we collected live-cell CLSM images of the ER at the cortex of BY-2 cells, i.e. optical sections of the ER parallel to the surface of the cell. Here, the ER is referred to as cortical ER and forms a well-defined polygonal network composed primarily of tubules interconnected by three-way junctions as well as sheet-like cisternae (40). As shown in the representative low-magnification images of Figure 2B, the fluorescent staining patterns attributable to both GFP-GPAT8 (top row) and GFP-GPAT9 (bottom row) generally overlap with RFP-ER. However, upon closer inspection at higher magnification both GFP-GPAT fusion proteins were clearly not evenly distributed throughout the ER. That is, similar to their distinct localization in subdomains of ER in transvacuolar strands observed in medial optical sections of fixed BY-2 cells (Figure 2A), GFP-GPAT8 and GFP-GPAT9 were often enriched in distinct (punctate) regions of the RFP-ER-labeled cortical ER (e.g. positions marked by solid arrowheads in Figure 2B). Interestingly, these regions did not appear to be limited to either tubular or cisternal ER or to the three-way junctions that join the tubular ER. Moreover, there were no obvious constrictions to the ER-lumenal space, as is frequently observed when, for instance, reticulon-type ER membrane proteins are expressed transiently in plant cells (reviewed in 10,47).

Finally, co-expression of a Cherry-fluorescent-protein-tagged version of GPAT8 (Cherry-GPAT8) and GFP-GPAT9 in living BY-2 cells demonstrated that the two GPAT proteins colocalized with each other in the same (punctate) regions of the cortical ER (Figure 2C, top row). This colocalization was further analyzed and quantified based on the mean Pearson's correlation coefficient r, which revealed a high degree of fluorescence signal overlap ($r = 0.75 \pm 0.10$; see *Materials and Methods* for additional details). Colocalization was also clearly evident in medial sections of formaldehyde-fixed BY-2 cells co-expressing different epitope-tagged versions of each protein, i.e. Myc-GPAT8 and HA-GPAT9, consisting of N-terminal-hemagglutinin (HA)-tagged GPAT9 (Figure 2C, bottom row; $r = 0.81 \pm 0.13$). Notably, the number and/or size of the ER subdomains labeled by GPAT proteins occasionally

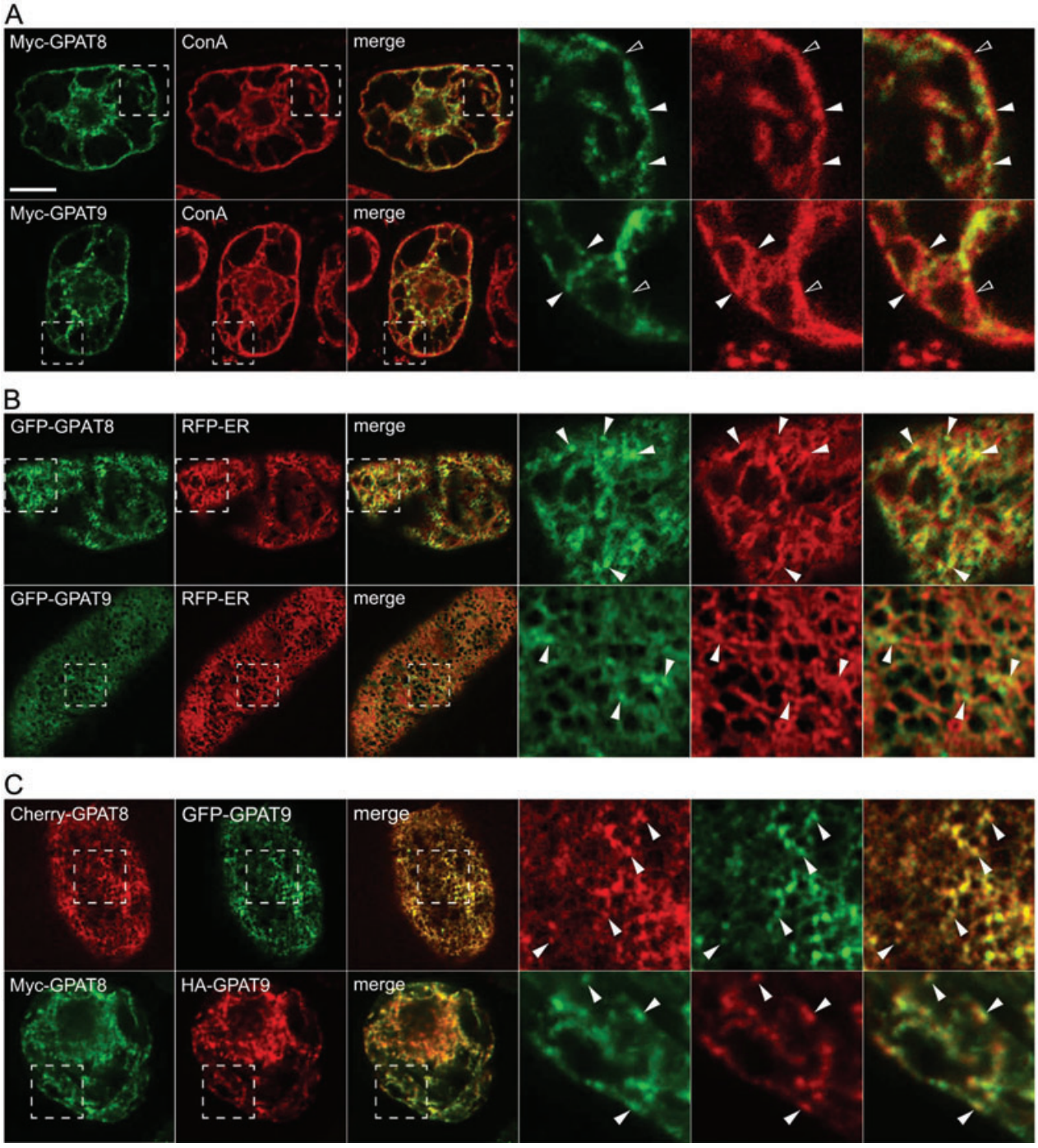

Figure 2: GPAT8 and GPAT9 are colocalized in distinct subdomains of ER. Subcellular localization of transiently (co-)expressed proteins was determined in either fixed or living tobacco BY-2 cells, using either GFP-, Cherry- or epitope-tagged (Myc or HA) fusion proteins and (immuno)CLSM. Combinations of (co-)expressed GPAT proteins or co-staining with Con A or RFP-ER (serving as markers of the ER) are indicated in each panel. Representative medial (mid-cell) optical sections of formaldehyde-fixed cells are shown in (A) and the bottom row of (C), while cortical sections (i.e. near the surface) of living (non-fixed) cells are shown in (B) and the top row of (C). Hatched boxes represent the portion of the cell shown at higher magnification in the panels to the right. The yellow/orange color in the merged images indicates colocalizations; white (solid) arrowheads indicate subdomains of ER enriched in GPAT proteins, while open arrowheads in (A) indicate regions of Con A-labeled ER containing low amounts of GPAT protein. Bar = 10 μm.

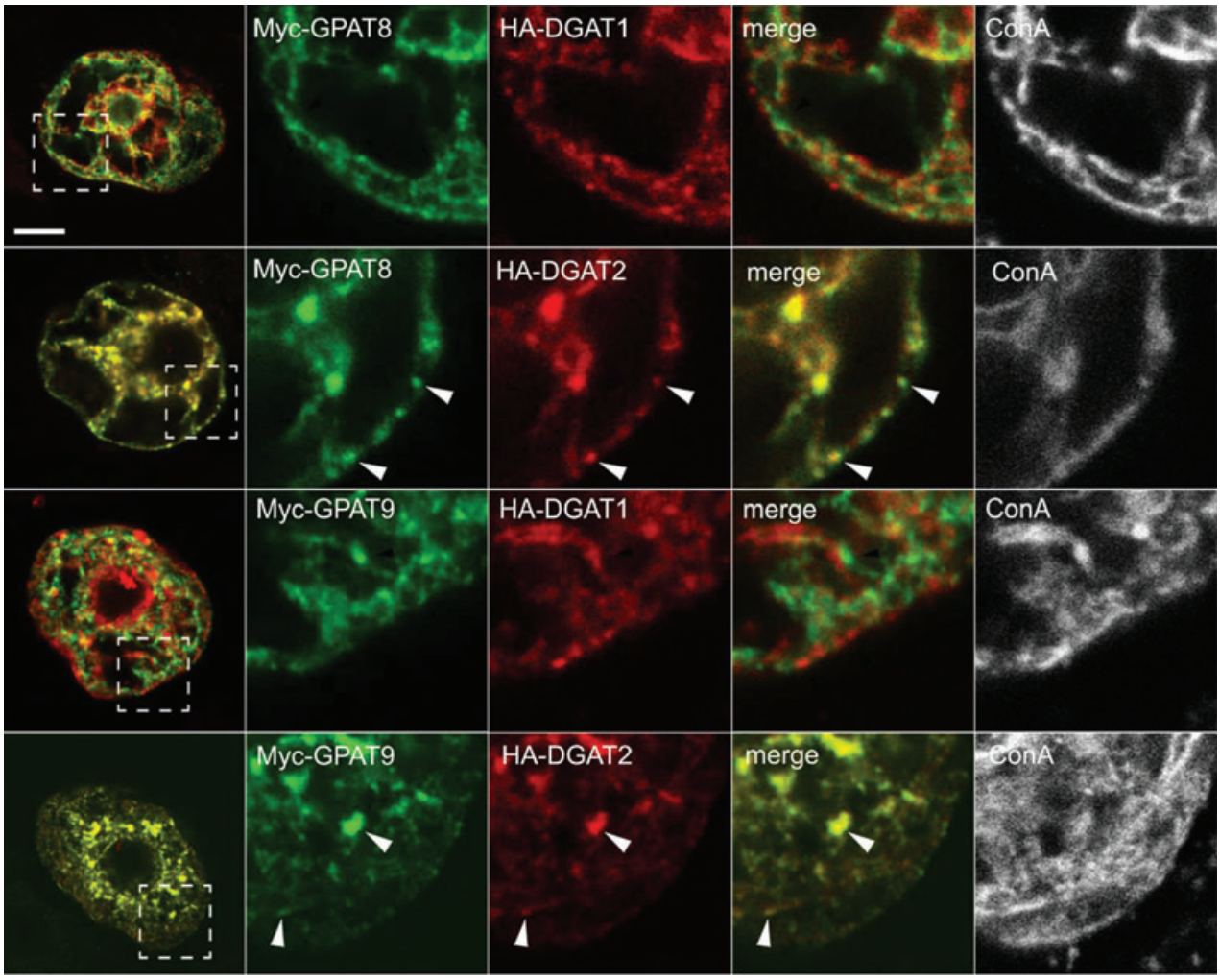

Figure 3: GPAT8 and GPAT9 are localized to the same subdomains as DGAT2. BY-2 cells expressing the indicated proteins were formaldehyde fixed, then analyzed by immunofluorescence CLSM of medial cell sections. Shown in the panels on the left are the (low magnification) merged images of the (green and red) fluorescence attributable to each pair of co-expressed proteins. The yellow/orange color in these images indicates colocalizations of co-expressed proteins. The hatched boxes represent the portions of the cells shown at higher magnification and as individual fluorescence micrographs in the panels to the right, including each co-expressed protein, the corresponding merged image and endogenous ER stained with Con A (pseudocolored white). White arrowheads indicate obvious colocalizations between co-expressed proteins in the same regions of the ER. Bar = 10 μm.

varied in transiently (co-)transformed cells, which might be because of their ectopic (over-)expression, their ability to form higher-ordered protein homo- and heterotypic interactions (see below) and/or the localized production of lipid metabolites.

Taken together, the results presented in Figures 2 and S3 indicate that the enrichment of GPAT proteins in certain regions (subdomains) of ER is likely a reflection of a biologically relevant process that is not dependent on the type of appended tags (either epitope or fluorescent protein) used in the experiment or, as already mentioned, because of the chemical fixation prior to viewing the cells. In the remainder of experiments described in this study, we chose to utilize medial optical sections of fixed BY-2 cells in order to evaluate protein subcellular localization(s), as ER architecture in this region of the BY-2 cell is less dense than in the cortical region (Figure 2; (40,42,48–52)), and as described below, this property was useful for visualizing and distinguishing multiple, different subdomains within the ER membrane.

The ER subdomains enriched in GPAT8 and GPAT9 are also occupied by DGAT2, but not DGAT1

Unlike the GPAT proteins described here (see Figure 2C), we previously demonstrated that tung DGAT1 and DGAT2 proteins are located in different subdomains of the ER (23). Thus, to determine if the subdomains occupied by GPAT8 and GPAT9 might be shared by DGAT1 or DGAT2,

Myc-tagged GPAT8 and GPAT9 proteins were each co-expressed individually with HA-tagged DGAT1 or DGAT2 proteins and colocalizations in BY-2 cells were determined by CLSM. As shown in Figure 3 (top row), co-expression of Myc-GPAT8 and HA-DGAT1 resulted in different staining patterns for each protein, indicating that the proteins were located in different subdomains of ER ($r = 0.20 \pm 0.06$). Co-expression of Myc-GPAT8 with HA-DGAT2, however, resulted in nearly identical staining patterns, with extensive colocalizations in the same regions of ER (white arrowheads; $r = 0.79 \pm 0.13$). Similarly, co-expression of GPAT9 with DGAT1 resulted in different staining patterns ($r = 0.22 \pm 0.08$), but co-expression with DGAT2 resulted in extensive colocalizations ($r = 0.86 \pm 0.11$) (Figure 3).

Collectively, these data indicate that tung GPAT8, GPAT9 and DGAT2 are located in similar subdomains of ER and that these regions of ER are distinct from those occupied by DGAT1. In the remainder of experiments described in this article, we chose to focus primarily on the targeting and assembly of the GPAT8 protein, as both GPAT8 and GPAT9 exhibited similar localization patterns, but transformation rates of transiently expressed GPAT8 in BY-2 cells were generally higher than those of GPAT9.

Split-Ub two-hybrid analysis in yeast cells revealed that GPAT8 interacts specifically with itself, GPAT9 and DGAT2, but not with DGAT1

The targeting of membrane-associated proteins to different subdomains of ER is a particularly interesting problem given the continuous nature of the ER membrane bilayer (40). As such, mechanisms must exist that allow the various proteins to distinguish between (and be enriched within) specific ER subdomains under steady-state conditions. To investigate whether protein–protein interactions might play a role in the localization of GPAT proteins to specific regions of the ER, we used the split-Ub-based membrane yeast two-hybrid assay to examine the interactions of GPAT8 with itself, GPAT9, DGAT1 and DGAT2. The split-Ub assay is similar in principle to the traditional two-hybrid assay in yeast cells except that protein–protein interactions can take place in cellular membranes (rather than the nucleus), which greatly improves the fidelity of measuring protein–protein interactions of membrane-associated proteins (illustrated in Figure 4A and reviewed in 53). From a practical standpoint, however, we found that it was essential to fuse Cub-LexA to the C-terminus of proteins to avoid false-negative results. For instance, in control experiments, we consistently observed that fusion proteins containing Cub-LexA linked to the C-terminus of P1, a passenger protein, yielded strong positive reporter gene activation when paired with the NubI control protein, whereas fusion proteins containing Cub-LexA linked at the N-terminus showed a significant decrease (or complete absence) of reporter gene activation when paired with NubI (data not shown). Although the basis for this 'polarity' effect is presently unknown, we have consistently observed similar results with many different Cub- or Nub-fusion proteins (data not shown) and similar results have been reported in the literature (54,55). As such, we did not include results from reciprocal testing of NubG and Cub on both the N- and C-termini of GPAT and DGAT proteins, as described below.

GPAT8 was fused with the Cub-LexA reporter at its C-terminus and co-expressed in yeast cells with Alg5-NubI, Alg5-NubG, NubG-GPAT8, NubG-GPAT9, NubG-DGAT1 and NubG-DGAT2 to test for protein–protein interactions. Alg5 is an endogenous yeast ER membrane protein (UDP-glucose:dolichyl-phosphate glucosyltransferase) that is involved in asparagine-linked glycosylation (57) and would not be expected to interact with GPAT8. As shown in Figure 4B, co-expression of GPAT8-Cub-LexA with Alg5-NubI resulted in significant reporter gene activation, as evidenced by the growth of the yeast strain on media lacking histidine and adenine. This result is expected, as the NubI moiety of Alg5 has high affinity for the Cub moiety on GPAT8, thereby activating the LexA-dependent reporter system. Co-expression of GPAT8-Cub-LexA with Alg5-NubG, however, resulted in no reporter gene activation, demonstrating that the GPAT8 and Alg5 proteins do not interact sufficiently to bring the Cub and NubG domains close together. No reporter gene activation was observed also when GPAT8-Cub-LexA was expressed with a soluble NubG domain (Figure 4B, NubG).

Co-expression of GPAT8-Cub-LexA with NubG-DGAT1 resulted in a low but detectable amount of reporter gene activation, suggesting that these proteins showed a weak interaction (Figure 4B). The amount of reporter gene activity was substantially increased, however, when GPAT8-Cub-LexA was co-expressed with NubG-DGAT2, suggesting that the interaction between GPAT8 and DGAT2 was significantly stronger than that of GPAT8 and DGAT1. There was also a small, but detectable amount of interaction between GPAT8-Cub-LexA and NubG-GPAT8 and NubG-GPAT9. These results were supported by qualitative β-galactosidase (β-gal) assays in which yeast cells were plated (in duplicate) on plates containing X-gal to induce blue color formation. As shown in Figure 4B (right panel), the change in colony color intensity was qualitatively similar to the results obtained from the prototrophic growth assay.

Although there was a clear difference in the amount of reporter gene activation between GPAT8 and DGAT2 in comparison to GPAT8 and DGAT1, there were much smaller differences in the reporter activation when comparing GPAT8-DGAT1 to GPAT8-GPAT8 or GPAT8-GPAT9 (Figure 4B). To help differentiate the strengths of the respective interactions, we performed a quantitative analysis of β-gal activity in cell lysates from each yeast strain and also normalized enzyme activity based on the steady-state amounts of the NubG-fusion proteins. The rationale for this was that protein–protein interactions are influenced in part by the abundance of each protein partner in the membrane. As shown in Figure 4C, the

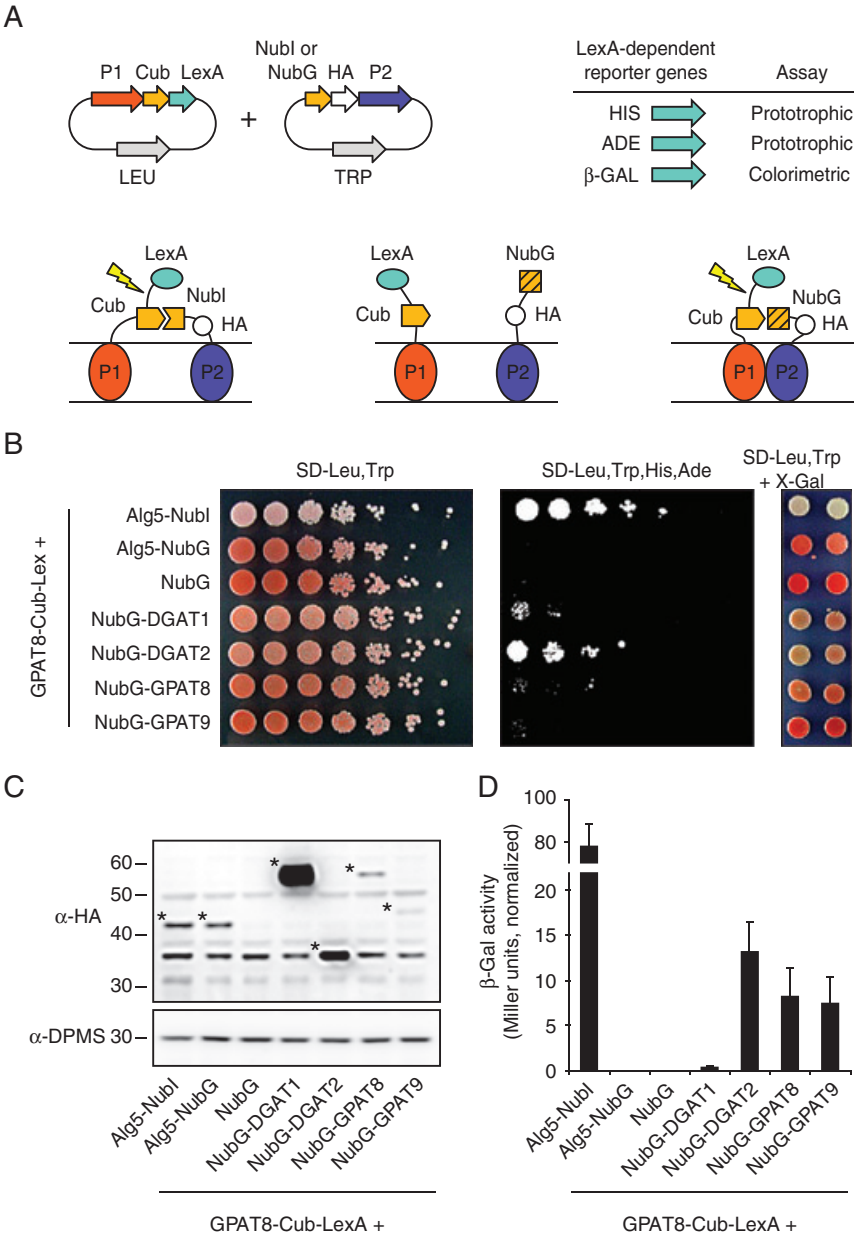

Figure 4: GPAT8 interacts with itself, GPAT9 and DGAT2, but not with DGAT1. A) Cartoon illustrating functional aspects of the split-Ub system. The DNA sequences encoding two different membrane proteins of interest (P1 and P2) are fused (in separate plasmids) to either the C-terminal half of ubiquitin (Cub) followed by the LexA transcription factor (plasmid on left) or the N-terminal half of ubiquitin (Nub, plasmid on the right) containing either the native Nub polypeptide sequence (NubI), which has high affinity for Cub, or a mutant form of Nub containing a point mutation (NubG), which has low affinity for Cub (56). The Nub constructs also carry an in-frame HA-epitope tag that is useful for determining the relative amounts of different Nub-containing fusion proteins by quantitative western blotting. Activation of the gene reporter system in yeast cells (including two prototrophic markers that allow the cells grow in the absence of histidine or adenine, as well as β-gal, for quantitative analysis) expressing a NubG-fusion protein is dependent on the ability of P1 and P2 to interact within a subcellular membrane, which brings the NubG and Cub domains into close proximity to allow cleavage and release of the soluble transcription factor, LexA. B) Prototrophic growth assay of yeast strains containing various combinations of GPAT8 co-expressed with several other protein partners. Serial dilutions of cells were plated on non-selective (left panel) or selective (right panel) media conditions. Note the appearance of robust growth on selective media by the yeast strain containing GPAT8 and the positive control protein Alg5-NubI, but no growth when GPAT8 is co-expressed with either Alg5-NubG or NubG. Note also the growth of yeast cells in the strain expressing GPAT8 and DGAT2, but not DGAT1. The corresponding qualitative β-gal plate assay, with the highest density of cells spotted twice, is shown to the right. C) Western blot analysis of the NubG-fusion proteins present in each yeast strain. The band of expected molecular mass for each NubG-fusion protein is marked with an asterisk. D) Quantitative β-gal assay of yeast cell lysates normalized by relative amounts of NubG-fusion proteins [determined from panel (C); see *Materials and Methods* for details].

steady-state amounts of the various NubG-fusion proteins did indeed vary between samples (as determined by western blotting of samples using an anti-HA antibody that recognized the HA-epitope tag present on each protein). Notably, the amounts of an endogenous ER membrane protein, dolichol-phosphate mannose synthase, did not vary appreciably between samples, indicating that these differences were not because of artifacts of protein loading. When β-gal activity of each yeast strain was quantified and normalized based on NubG-fusion protein amounts, the results (presented as a bar graph in Figure 4D) were fairly similar to the qualitative data presented in Figure 4B, with the exception that the amount of β-gal activity for GPAT8-DGAT2, GPAT8-GPAT8 and GPAT8-GPAT9 combinations were clearly higher than that of GPAT8-DGAT1. Taken together, the results presented in Figure 4 show that GPAT8 shows a selective interaction with itself, GPAT9 and DGAT2, but not DGAT1, and as these interactions are similar to the observed colocalizations in BY-2 cells (Figures 2 and 3), it is possible that protein–protein interactions contribute to the biogenesis of GPAT/DGAT2 subdomains within the ER membrane.

The targeting of GPAT8 to ER subdomains involves hydrophobic regions of the protein

Subsequently, we determined whether there were specific regions of the GPAT8 protein that were responsible for its targeting to ER subdomains. Toward this end, a series of Myc-GPAT8 deletion mutants were constructed and their localization in transformed BY-2 cells was determined by CLSM (Figure 5). As shown in Figure 5B (top row), expression of the C-terminal half of GPAT8 (i.e. residues 272–503; GPAT8-Myc 272-503), which includes the acyltransferase domain, resulted in a diffuse cytosolic fluorescence pattern that was distinct from the reticular fluorescence pattern attributable to Con A-stained ER, indicating that this region of GPAT8 alone is insufficient for ER subdomain localization. In contrast, expression of either the N-terminal half of GPAT8 (residues 1–270), which included both of the protein's two predicted hydrophobic regions (residues 50-89 and 246-268, illustrated as black bars in Figure 5A; refer also to Figure S1), or the N-terminal half of GPAT8 without its N-terminal soluble region (residues 1–50), resulted in both mutant proteins (i.e. Myc-GPAT8 1-270 and Myc-GPAT8 51-270) being localized to (punctate) ER subdomains in a manner similar to that observed for the full-length Myc-GPAT8 protein (compare Figures 2A and 5B). Localization to ER subdomains was also observed when most of the soluble region between the two predicted hydrophobic regions was deleted in the context of the Myc-GPAT8 51-270 mutant (i.e. Myc-GPAT8 51-270Δ110-224) (Figure 5B), indicating that the targeting information in GPAT8 is contained primarily within its hydrophobic regions. However, Myc-GPAT8 94-270, containing only the second hydrophobic region (residues 246–268) and flanking soluble regions, localized to the cytosol and primarily throughout the 'general' ER. That is, Myc-GPAT8

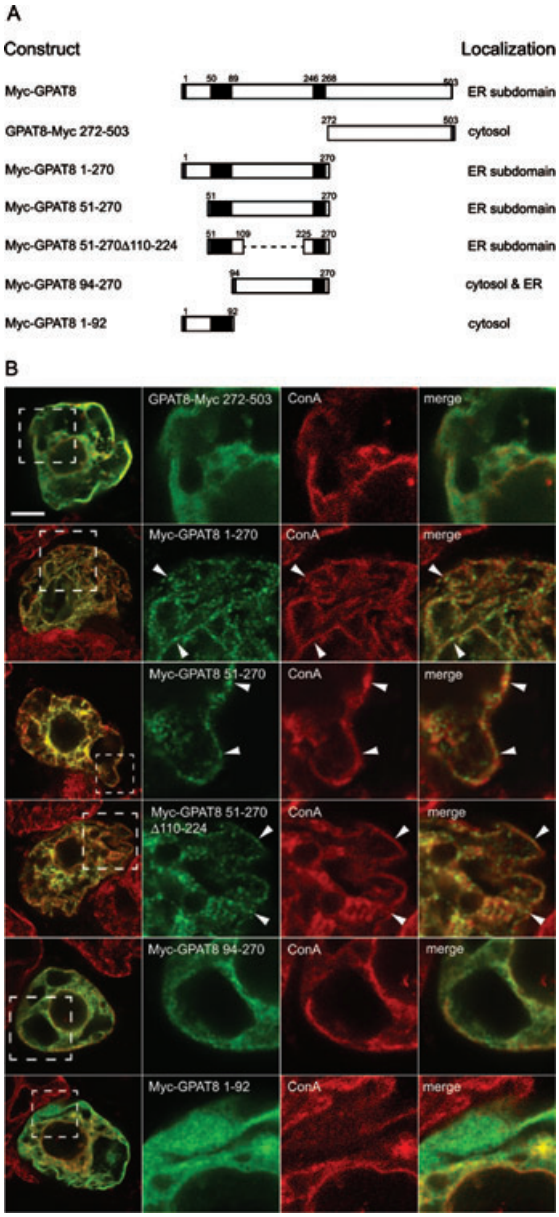

Figure 5: The GPAT8 subdomain targeting signal is located in hydrophobic regions of the protein. A) Schematic representations of full length and various Myc-GPAT8 truncation mutants and their corresponding subcellular localizations in transformed BY-2 cells. Numbers in the name of the construct denote the specific amino acid residues derived from full-length (503 residues) GPAT8. Black boxes denote the positions of the N- or C-terminal-appended Myc epitope tag and putative hydrophobic regions in GPAT8 (residues 50–89 and 246–268). The stippled line in the illustration of Myc-GPAT8 51-270Δ111-224 represents the portion of the soluble loop region that was deleted (residues 110–224) in this construct. B) Representative immunofluorescence CLSM micrographs of BY-2 cells transiently transformed with individual Myc-GPAT8 truncation mutants, all of which are illustrated in (A). Cells were processed and micrographs labeled as described in Figure 3. White arrowheads indicate obvious examples of expressed mutant proteins being localized to distinct regions of the Con A-stained ER. Bar = 10 μm .

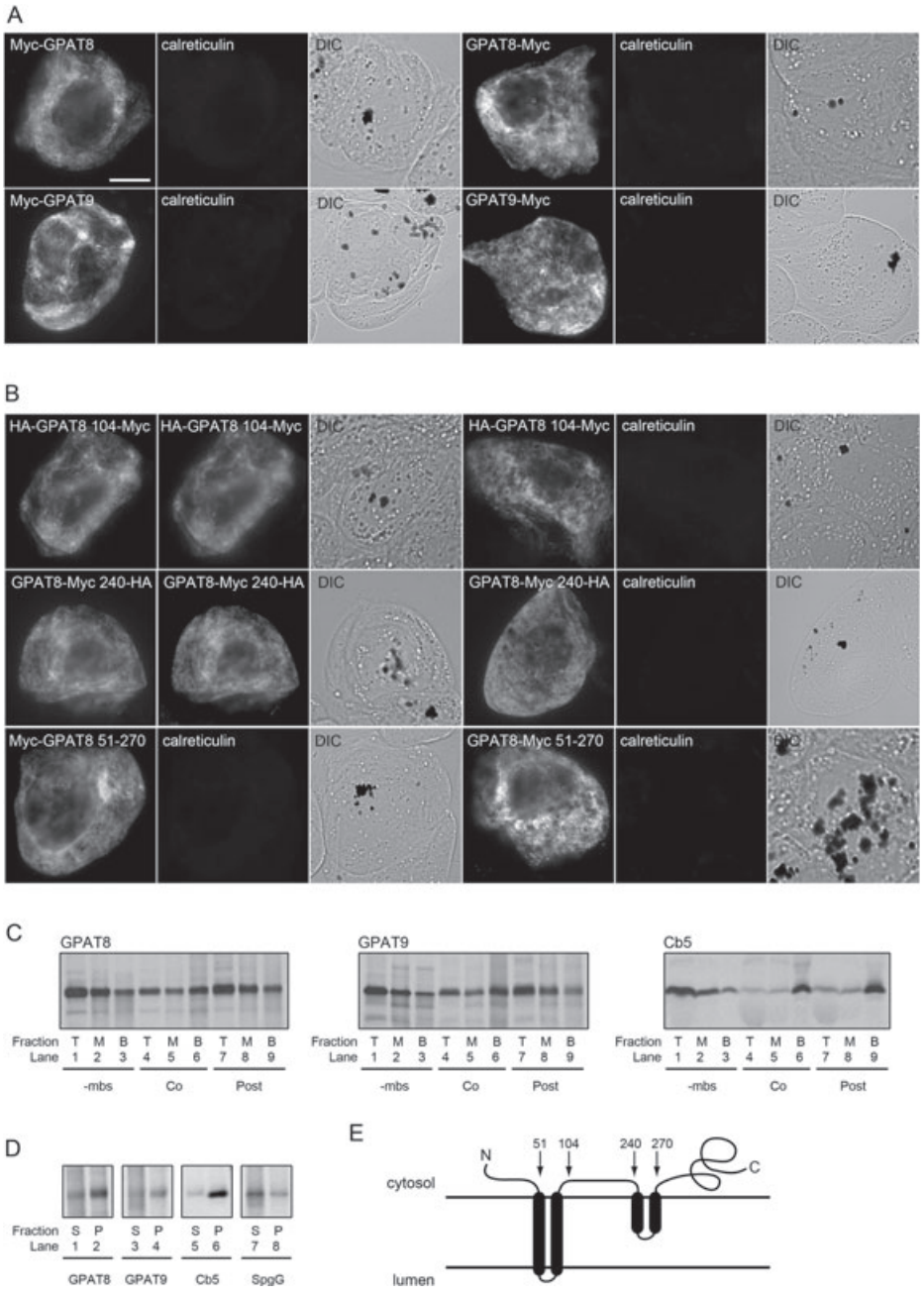

Figure 6: Legend on next page.

94-270, unlike Myc-GPAT8 51–270, for instance, appeared to be distributed more uniformly throughout the Con A-stained ER, rather than mostly to distinct subdomains (Figure 5B). These latter data indicate that the second hydrophobic region in GPAT8 is capable of associating with ER membranes in a general sense, but lacks the targeting information required for efficient trafficking to ER subdomains. Interestingly, Myc-GPAT8 1-92, which includes the N-terminal 92 amino acid residues of the protein containing the first hydrophobic region (residues 50–89), localized almost exclusively to the cytosol, as evidenced by the overall diffuse-like fluorescence attributable to this mutant protein (Figure 5B, compare with fluorescence attributable to other ER-localized GPAT8 mutants). Similar cytosolic localization was also observed for Myc-GPAT8 1-160, which (compared to Myc-GPAT8 1-92) includes an additional 71 residues after the first hydrophobic region (data not shown). Taken together, the results presented in Figure 5 suggest that both of the predicted hydrophobic regions in GPAT8 are required for its proper association with ER membranes and for trafficking to specific ER subdomains.

GPAT8 and GPAT9 are integral membrane proteins with the majority of protein sequence oriented toward the cytosol

Subsequently, we determined whether the changes in subcellular localization of the various truncation mutants described above (Figure 5) resulted also in changes to the protein–protein interaction profile of GPAT8. Before the split-Ub experiments could be conducted, however, it was necessary to obtain more information regarding the topology of the GPAT proteins in ER membranes. That is, for the split-Ub reporter system to work properly, the NubG and Cub-LexA moieties present on the two membrane proteins (P1 and P2) must be located on the same (cytosolic) side of the organellar membrane (53).

We previously mapped the topological orientation of full-length DGAT1 and DGAT2 from tung tree (23) and GPAT8 and GPAT9 from *Arabidopsis* (30) and demonstrated that the N- and C-termini of both sets of proteins were located in the cytosol. Here, we confirmed that the tung GPATs adopt similar topologies as their *Arabidopsis* counterparts in ER membranes. As shown in Figure 6A, expression of N- or C-terminal epitope-tagged versions of tung GPAT8 and GPAT9 in BY-2 cells, followed by differential permeabilization with digitonin, which perforates only the plasma membrane and not organellar membranes (58), revealed that both epitope tags were immunodetectable (via epifluorescence microscopy) in the cytosol. To obtain additional topological information for GPAT8, we determined the topology of the polypeptide sequence either before or after each of the two predicted hydrophobic regions within the context of either full-length GPAT8 or the GPAT8 51-270 truncation mutant. The constructs tested included two double-epitope-tagged versions constructed in the context of the full-length protein: (i) HA-GPAT8 104-Myc, containing an N-terminal HA tag and a Myc tag inserted at amino acid position 104, just downstream of the first predicted hydrophobic region (residues 50–89) and (ii) GPAT8-Myc 240-HA, containing a C-terminal Myc tag and an HA tag inserted

Figure 6: GPAT8 and GPAT9 are co-translationally inserted, integral membrane proteins that are orientated with the majority of their sequence exposed to the cytosol. A and B) Representative micrographs of BY-2 cells transiently transformed with either (A) N- or C-terminal-appended Myc-tagged-versions of GPAT8 or GPAT9 or (B) HA-GPAT8 104-Myc, GPAT8-Myc 240-HA or Myc-GPAT8 51-270 or GPAT8-Myc 51-270. Cells were then fixed in formaldehyde at approximately 4 h after biolistic bombardment, permeabilized using digitonin, which selectively permeabilizes the plasma membrane only (58) and processed for (immuno)epifluorescence microscopy. Each micrograph is labeled at the top left with the name of either the expressed (double) epitope-tagged full-length or mutant (truncated) GPAT8 protein or calreticulin, an endogenous intra-organellar (i.e. ER lumenal) protein serving as a negative control (30,59). Also shown for each set of immunostained cells is the corresponding differential interference contrast (DIC) image. Note that the presence of immunostaining in digitonin-permeabilized cells indicates that the expressed protein's appended epitope tag(s) is exposed to the cytosol. Conversely, endogenous calreticulin is not immunodetectable in the same corresponding digitonin-permeabilized cells. Note also in (B) that cells expressing either HA-GPAT8 104-Myc or GPAT8-Myc 240-HA were incubated with both anti-HA and anti-Myc antibodies (left two panels) or anti-Myc or anti-HA and anti-calreticulin antibodies (right panels). Bar = 10 μm. C) Co-translational insertion of GPAT proteins into ER membranes *in vitro*. Plasmids containing sequences encoding either GPAT8, GPAT9 or Cb5 were transcribed *in vitro* and the resulting RNA products were either: co, translated in reticulocyte lysate containing canine pancreatic microsomes; post, microsomes were added after the reticulocyte lysate translation reactions were terminated with cycloheximide or -mbs, no microsomes were added to the reticulocyte lysate translation reactions. All reactions were layered on top of a sucrose cushion and microsomes were pelleted by centrifugation as described in the *Materials and Methods*. The resulting samples were then divided into top (T), middle (M) and bottom (B) fractions and equivalent percentage volumes of each fraction were analyzed by SDS–PAGE. D) Membrane integration of GPAT and control proteins. Microsome-associated proteins (bottom fraction from *in vitro* translation assay) were resuspended in sodium carbonate (pH 11.5) and then lumenal and peripheral proteins (S) were separated from integral membrane proteins (P) by centrifugation. Equivalent percentage volumes of each fraction were then analyzed by SDS–PAGE. Note that the amount of GPAT9 protein in lanes 3 and 4 is not the same as for GPAT8 because the recovery of the GPAT9 protein pellet [lane 6 in (C)] was not as good, in this case, as it was for GPAT8. Regardless, the results presented in (C) and (D) are representative of three independent experiments. E) Topology model for GPAT8 in the ER membrane. Based on the results presented in (A–D), GPAT8 is depicted to be integral membrane protein with the majority of its polypeptide sequence, including its N- and C-termini, orientated toward the cytosol. The protein is also considered to be anchored by two hydrophobic regions: the first region (residues 50–89) containing two putative TMDs, whereas the second region (residues 246–268) only partially spans the ER membrane. The relative amino acid positions of epitope tag sequences appended to modified (truncated) versions of GPAT8 described in (B) are indicated with down arrows.

at amino acid position 240, just before the second predicted hydrophobic region (residues 246–268). We also examined the topology of two related versions of the GPAT8 51-270 mutant: (i) Myc-GPAT8 51-270, which, as described above (Figure 5), contains a Myc tag, the beginning of the first hydrophobic region and (ii) GPAT8-Myc 51-270, which contains a Myc tag just after the second hydrophobic region. As shown in Figure 6B, expression of these four (full length or mutant) GPAT8 proteins individually in BY-2 cells followed by differential permeabilization with digitonin revealed that each of the appended epitope tags, but not the endogenous ER-lumenal protein calreticulin in the same cells, was immunodetectable, indicating that the epitopes in these regions of GPAT8 are all exposed on the cytosolic side of ER membranes.

As a control to ensure that the cytosolic localization of the epitope tags in all the GPAT proteins described above was not simply an artifact of the transient expression system, we also analyzed the topology of N- or C-terminal-Myc-tagged versions of Cb5 reductase (CBR) in BY-2 cells. Consistent with the previously reported topology of this type I ($N_{lumen}-C_{cytosol}$) ER membrane protein (59), transiently expressed CBR-Myc (consisting of CBR appended to Myc at its C-terminus) and endogenous cytosolic α-tubulin, but not expressed Myc-CBR (CBR appended to Myc at its N-terminus), were immunodetectable in digitonin-permeabilized cells (Figure S4A). However, both expressed CBR-Myc and Myc-CBR, as well as endogenous calreticulin, were immunodetectable when cells were permeabilized with Triton-X-100, a detergent that perforates both plasma membrane and organellar membranes (58) (Figure S4A). Likewise, in non-transformed, digitonin-permeabilized BY-2 cells, endogenous α-tubulin, but not endogenous calreticulin, was immunodetectable, whereas both proteins were immunodetectable when permeabilized with Triton-X-100 (Figure S4B), as expected (30,58,59).

The results described above indicated that the majority of GPAT8 protein sequence was localized on the cytosolic side of ER membranes. To determine whether the protein was integrally or peripherally associated with ER membranes, we used *in vitro* transcription/translation reactions with ER-derived microsomes to determine if the protein was inserted co- or post-translationally into ER membranes and whether any of the membrane-associated protein was resistant to extraction with alkaline sodium carbonate, which differentiates peripheral from integral membrane binding. As shown in Figure 6C, inclusion of microsomal membranes during the transcription/translation reaction (co) resulted in cofractionation of a significant proportion of GPAT8 or GPAT9 protein with membranes (bottom fractions), while significantly less GPAT8 or GPAT9 protein was cofractionated with membranes when the microsomes were added after the transcription/translation reaction had been terminated (post). Indeed, the amount of GPAT8 or GPAT9 recovered in the bottom fractions from post-translational reactions was more similar to the amounts obtained when no membranes (-mbs) were included in the transcription/translation reactions (Figure 6C), indicating that, rather than binding to membranes, a portion of the GPAT proteins had misfolded and/or aggregated, a common behavior for proteins synthesized by *in vitro* transcription/translation. Shown also in Figure 6C are the results of control experiments with rat liver Cb5, which inserts post-translationally into the ER (60,61), confirming the competence of the microsomes used in the co- or post-translational assays. Resuspension of the membrane fractions with 0.1 M sodium carbonate (pH 11.5), to remove lumenal and peripherally associated proteins, followed by re-centrifugation to isolate membranes (and integrally associated proteins), was used to determine whether the GPAT proteins integrated into the microsomal membranes. Indeed, as shown in Figure 6D, the majority of both GPAT8 and GPAT9 (albeit to a lesser extent for GPAT9) was recovered in the pellet (P) fraction. Likewise, the majority of the control integral membrane protein Cb5 was recovered in the pellet fraction after sodium carbonate extractions (Figure 6D). In contrast, most of the lumenal control protein SpgG, which consists of the signal sequence from the luminal ER protein preprolactin fused to a portion of the well-characterized passenger protein glycoglobin, was released from and therefore did not pellet with the membranes, as expected (60).

Taken together, the data presented in Figure 6A–D support a topology model for GPAT8 in which, following its co-translational synthesis on ER membranes, the majority of the protein, including the N- and C-termini, as well as the acyltransferase domain (residues 306–407), is located in the cytosol, and that the protein is integrated into the membrane by two hydrophobic regions (Figure 6E). The first hydrophobic region (residues 50–89) is long enough to include two putative transmembrane-spanning α-helices, whereas the second hydrophobic region is shorter (residues 246–268), and thus was assigned as a short hairpin-like structure in the membrane. Notably, this region contains a conserved proline knot motif (i.e. -LPF-, refer also to Figure S1) that could induce the formation of a hinged or kinked region in this protein segment (62). Although further experimentation is required to elucidate the precise topology of the GPAT proteins, the results obtained in this study indicate at least that the N- and/or C-termini of the native proteins, as well as all of the GPAT8 truncation mutants that were tested for their protein–protein interactions (see below), are present in the cytosol, and as such, are suitable for the analysis using the split-Ub assay.

Split-Ub analysis and protein localization studies help to identify an ER subdomain targeting signal within the first hydrophobic region of GPAT8

The first GPAT8 mutant tested in terms of its protein–protein interaction profile was GPAT8 51-270, which

contains both of the hydrophobic regions in the N-terminal half of GPAT8 that were shown to be sufficient for targeting to ER subdomains (Figure 5B). As shown in Figure 7A, the protein–protein interaction profile of GPAT8 51-270 was slightly different in comparison to the full-length protein. That is, this truncation mutant retained the ability to selectively interact with DGAT2 in comparison to DGAT1, but its overall level of interaction with GPAT8 or GPAT9 was significantly reduced. These results suggest that the missing portions of GPAT8 51-270 (i.e. the N-terminal 50 amino acid residues and/or the C-terminal half of the protein that contains the soluble acyltransferase domain) are necessary for the observed protein–protein interactions between full-length GPAT8 and itself and/or GPAT9.

A similar examination of GPAT8 94-270, however, revealed that this mutant protein, which contains only the second hydrophobic region of the protein, no longer interacted appreciably with DGAT1, DGAT2, GPAT8 or GPAT9, but still interacted with the positive control Alg5-NubI (Figure 7A, middle panel), suggesting that the second hydrophobic region of the GPAT8 protein is not sufficient to account for the observed interaction between GPAT8 51-270 and DGAT2 (left panel). However, the GPAT8 1-92 mutant protein, which contains just the first hydrophobic region of GPAT8, displayed a strong and selective interaction with DGAT2, but not with DGAT1, GPAT8 or GPAT9 (Figure 7A, right panel).

Given the high level of protein–protein interaction detected between the GPAT8 1-92 mutant and DGAT2 (Figure 7A), we tested whether co-expression of Myc-GPAT8 1-92 and HA-DGAT2 in BY-2 cells might redirect the former protein from the cytosol to DGAT2-containing ER subdomains. As shown in Figure 7B (top row), Myc-GPAT8 1-92 was indeed localized to DGAT2-enriched subdomains (white arrowheads) when co-expressed with HA-DGAT2 ($r = 0.79 \pm 0.09$). This mutant protein was not, however, recruited to DGAT1-containing ER subdomains when co-expressed with HA-DGAT1 (bottom row; $r = 0.24 \pm 0.10$), but rather localized mostly throughout the cytosol in a manner similar to when expressed on its own (compare Figures 5B and 7B).

Collectively, the results presented in Figure 7 demonstrate that the first hydrophobic region of GPAT8 contains a protein interaction signal that allows for high-affinity interaction with the DGAT2 protein (as measured in the split-Ub assay), and that co-expression of GPAT8 1-92 with DGAT2 in BY-2 cells is sufficient to recruit this mutant protein to DGAT2-enriched ER subdomains.

An amphipathic helix-like motif within the first hydrophobic region of GPAT8 is important for interaction with DGAT2 and targeting to ER subdomains

The first predicted hydrophobic region within the GPAT8 1-92 mutant protein sequence spans at least 40 amino acids (residues 50–89, shaded gray in Figure 8A; refer also to Figures 6E and S1) and contains up to two sequences that have the propensity to form an α-helical transmembrane domain (TMD). However, the assignment of specific TMD(s) in this region using online algorithms such as TMHMM, TOPCONS or TMPRED was not always consistent (data not shown). As such, we took a more unbiased approach to analyzing the targeting information in this region by constructing two substitution mutants that, as illustrated in Figure 8A, replaced either the first half (residues 50–69) or the second half (residues 67–89) of the hydrophobic region with a different hydrophobic sequence derived from the first predicted TMD (TMD1) of tung DGAT1 (23). The mutants were then characterized by split-Ub and subcellular localization. The rationale for choosing the DGAT1 TMD1 for this experiment was twofold. First, if any sequence- or motif-specific information in the first hydrophobic region of GPAT8 is responsible for interaction with DGAT2, then a similar hydrophobic sequence of different amino acid composition should disrupt this protein–protein interaction. Second, substitution of the first hydrophobic region in the context of the GPAT8 1-92 mutant with the DGAT1 TMD would also allow us to investigate whether this region in DGAT1 plays a similar role in TMD-dependent protein–protein interactions and/or protein localization to DGAT1-enriched ER subdomains.

As shown in Figure 8B (left panel), replacement of the second half of the hydrophobic region (residues 67–89) with TMD1 from DGAT1 had essentially no effect on the ability of the modified mutant protein (i.e. GPAT8 1-92-Mut1-Cub-LexA) to selectively interact with DGAT2 in the split-Ub assay [compare Figures 8B (left panel) and 7A (right panel)]. Moreover, Myc-GPAT8 1-92-Mut1, similar to Myc-GPAT8 1-92 (Figure 7B), was efficiently recruited to ER subdomains (white arrowheads) in BY-2 cells when co-expressed with HA-DGAT2 (Figure 8C, top row; $r = 0.73 \pm 0.10$). In contrast, replacement of the first half of the hydrophobic region (residues 50–69) with the DGAT1 TMD1 substantially reduced the ability of the modified mutant protein to interact with DGAT2 (Figure 8B, right panel), and was also inefficiently recruited to ER subdomains when co-expressed with DGAT2. That is, Myc-GPAT8 1-92-Mut2 localized mostly to the cytosol when co-expressed with HA-DGAT2 in BY-2 cells (Figure 8C, bottom row; $r = 0.46 \pm 0.11$). Notably, both GPAT8 1-92-Mut1 and -Mut2, similar to their wild-type mutant protein counterpart, localized to the cytosol in BY-2 cells when expressed on their own and neither mutant protein interacted appreciably with DGAT1 in the split-Ub assay (Figure 8B) nor was recruited to DGAT1-enriched ER subdomains when co-expressed with HA-DGAT1 (data not shown). Taken together, these results indicate that the first half of the hydrophobic region in GPAT8, which includes an amphipathic helix-like motif (see *Discussion*), is required for both efficient interaction with the DGAT2 protein and for DGAT2-dependent relocalization to ER subdomains in plant cells.

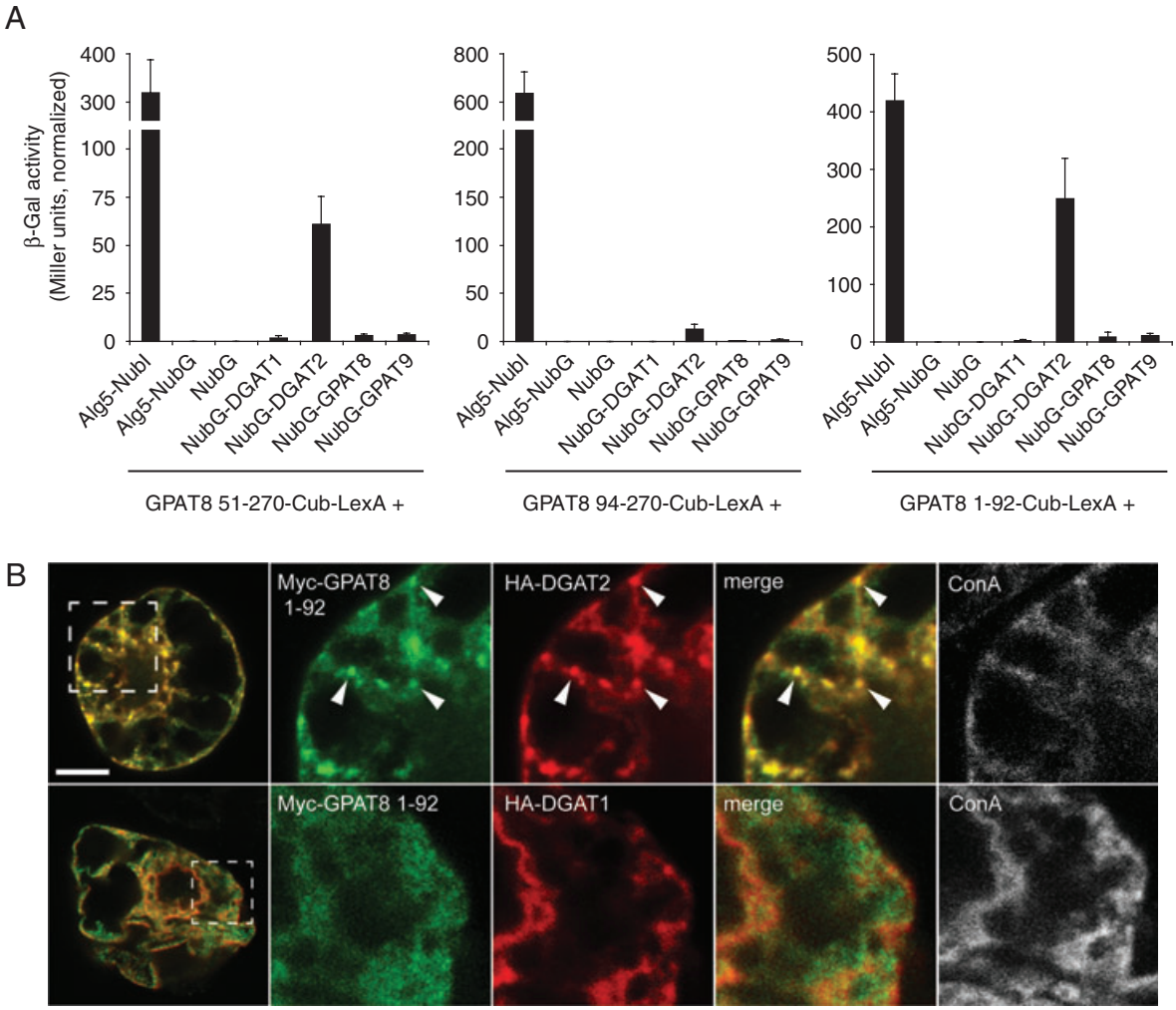

Figure 7: The N-terminal hydrophobic region of GPAT8 contains a signal for both interaction with DGAT2 and for DGAT2-dependent colocalization in ER subdomains. A) Protein–protein interactions were evaluated using the split-Ub quantitative β-gal assay, as described in Figure 4. Strains and plasmid combinations are shown along the bottom. B) Representative micrographs of BY-2 cells transiently co-transformed with Myc-GPAT8 1-92 and HA-DGAT2 or HA-DGAT1, then processed for immunofluorescence CLSM as described in Figure 3. White arrowheads indicate obvious colocalizations between co-expressed Myc-GPAT8 1-92 and HA-DGAT2 in the same regions of the ER. Bar = 10 μm.

Discussion

Localization of GPAT8 and GPAT9 to subdomains of ER

The ER is a dynamic organelle both structurally and functionally, consisting of a complex network of sheets and tubules that participate in numerous essential metabolic functions, including co-translational protein synthesis, protein secretion via vesicular transport and the synthesis of various storage compounds such as the oils and proteins found in plant seeds (10). Although there is increasing appreciation that these activities are carried out by specific collections of proteins and enzymes located in distinct or specialized regions of the ER, the molecular mechanisms by which these functional 'subdomains' are assembled and maintained, as well as their composition and distribution, are not well understood. How membrane proteins are trafficked to specific regions of ER, in particular, is a challenging question as the ER membrane is a continuous two-dimensional bilayer that supports both passive and active diffusion (40). As such, many of the current working models for ER subdomain biogenesis rely on the principles of protein self-assembly, whereby the ability of specific membrane proteins to distinguish between various ER subdomains and also to be maintained in these distinct regions under steady-state conditions is based primarily on their homotypic- and heterotypic-binding properties (7,13,24,25). ER subdomain biogenesis may also rely on thermodynamically sensitive lateral partitioning of proteins within the lipid bilayer, for instance,

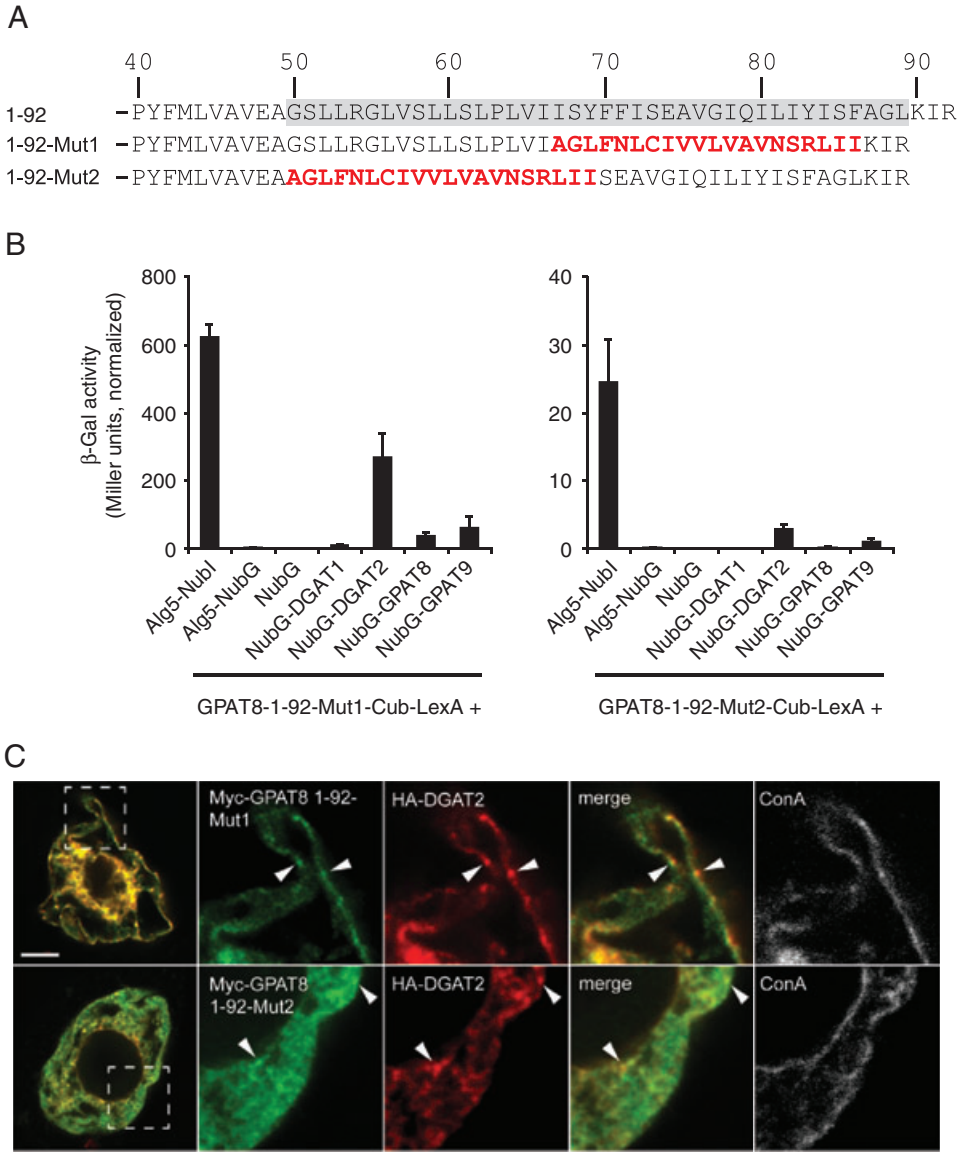

Figure 8: The first half of the N-terminal hydrophobic region of GPAT8 is essential for binding DGAT2 and DGAT2-dependent colocalization in ER subdomains. A) Deduced amino acid sequences at the C-terminal end of Myc-GPAT8 1-92 and mutant versions thereof. Numbers shown above the GPAT8 1-92 sequence represent their relative position in full-length GPAT8 and the putative hydrophobic region (residues 50–89) is shaded in gray. Bold and red colored amino acids in the sequences of the mutant versions of Myc-GPAT8 1-92, namely 1-92-Mut1 and 1-92-Mut2, are those derived from the first predicted TMD of DGAT1 (residues 128–147; (23)). B) Protein–protein interactions were evaluated using the split-Ub quantitative β-gal assay, as described in Figure 4. Strains and plasmid combinations are shown along the bottom. C) Representative micrographs of BY-2 cells transiently co-transformed with Myc-GPAT8 1-92-Mut1 or Myc-GPAT8 1-92-Mut2 and HA-DGAT2, then processed for immunofluorescence CLSM as described in Figure 3. White arrowheads indicate obvious colocalizations between co-expressed proteins in the same regions of the ER. Bar = 10 μm.

through interaction(s) of protein TMD(s) with specific membrane lipids or lipid microdomains. For instance, protein localization in so-called 'lipid rafts' appears to require TMDs of sufficient length to partition into these distinct membrane regions (63), while the TMDs of reticulon-type proteins are thought to form a 'W'-shaped structure that results in targeting to and enrichment within highly curved regions of ER membranes (i.e. tubular ER) (10,47).

Here we provide insight to the biogenesis of two different subdomains of the ER, both of which contain enzymes associated with lipid metabolism. That is, while we previously showed that the DGAT1 and DGAT2 enzymes from plants are found in different regions of ER (23), we demonstrate here that two GPAT-like enzymes (tung GPAT8 and GPAT9) colocalize with each other (Figure 2) and with DGAT2 in subdomains of ER, but not with DGAT1 (Figure 3). We showed also using the

split-Ub-based membrane yeast two-hybrid system that subdomain-specific, protein–protein interactions could be detected between GPAT8 and itself, GPAT9 and DGAT2, but not with DGAT1 (Figure 4). Combined, these results suggest that, similar to mechanisms proposed to underlie the formation of other ER subdomains, homo- and heterotypic protein–protein interactions play an important role in the biogenesis of GPAT- and DGAT-containing ER subdomains. Although we identified a specific region of the GPAT8 protein involved in binding to DGAT2 (see below), we currently do not know which region of GPAT8 is responsible for interacting with itself. Nevertheless, multiple protein–protein interaction sites are commonly found in many protein constituents of complexes such as 'scaffolding' proteins involved in signal transduction pathways (64). Thus, if there are two different regions of GPAT8 involved in mediating homo- and heterotypic interactions, then a simple model for subdomain biogenesis can be envisioned, whereby homotypic protein association would result in protein oligomerization, which would provide multiple binding sites for subsequent recruitment of heterotypic protein partners. Consistent with this premise, the N-terminal region of *Brassica* and mammalian DGAT1 has been shown to mediate the homotypic oligomerization of these two proteins (65,66).

Although it is currently unknown if thermodynamic (e.g. protein–lipid) partitioning also plays a role in GPAT localization, it is notable that the membrane topology and protein structural features of GPAT8 are somewhat analogous to reticulon-type proteins. For instance, both types of proteins adopt similar topologies wherein the majority of protein structure is found on the cytosolic side of ER membranes and have two hydrophobic regions that each contain TMDs predicted to form hairpin structures (Figure 6E and (51,67)). However, despite these similarities, there are also conspicuous differences in the ER subdomain properties of these proteins. For instance, the GPAT (and DGAT)-containing ER subdomains are not restricted to tubular ER (like those of reticulons; (68)), but rather appear to be distributed throughout the entire ER network, including the nuclear envelope (Figures 2, 3 and S3). In addition, transient expression of GPATs, while perhaps inducing some alterations in ER appearance (Figures 2, 3 and S3), consistent with the ectopic expression of other ER membrane proteins involved in lipid biosynthesis (23,30,41,69), does not cause the types of restrictions or 'pocketing' of the ER-lumenal space that is frequently observed with transiently expressed reticulons (10,47). Thus, there must be some key differences that account for the distinct targeting properties of each protein type within ER membranes. One possibility, as discussed below, is the presence of a putative amphipathic helical structure within the first hydrophobic region of GPAT8.

Although the localization of GPAT8, GPAT9 and DGAT2 in the same subdomains of ER suggests that these proteins are functionally related, there is currently no biochemical evidence regarding the role of these GPAT enzymes in tung oil biosynthesis. Moreover, while the GPAT9 homolog in mammalian cells has been demonstrated to play an important role in TAG biosynthesis (36,70), the GPAT8 homolog in *Arabidopsis* has been shown to play a role in the synthesis of lipids destined for the plant cuticle (34). It is not appropriate, therefore, to directly infer the biochemical function(s) of tung GPAT8 and GPAT9 enzymes based on the sequence information alone. As such, the cell biology experiments described here should help guide future biochemical and genetic studies focused on elucidating the role of these and other GPAT enzymes in plant lipid metabolism.

Potential role of amphipathic helices in subdomain biogenesis

Although the strong interaction of the GPAT8 1-92-Cub-LexA [which contains just the first predicted hydrophobic region (residues 50–89) of GPAT8] with NubG-DGAT2 in the split-Ub yeast two-hybrid assay (Figure 7) was somewhat surprising given that this mutant protein was localized to the cytosol when expressed alone in BY-2 cells (Figure 5), it is well known that the split-Ub system can function with either cytosolic and/or membrane-bound interacting protein partners (53,56). Thus, it is entirely reasonable that soluble GPAT8 1-92-Cub-LexA interacted with membrane-bound NubG-DGAT2 in our split-Ub assay. Furthermore, we confirmed via differential detergent permeabilization experiments that the Myc-GPAT8 1-92 mutant protein when co-expressed with HA-DGAT2 in BY-2 cells adopted a similar orientation in ER subdomains to that of full-length GPAT8, i.e. the N-terminal-appended Myc epitope of Myc-GPAT8 1-92, similar to that of full-length Myc-GPAT8 (Figure 6A), was oriented toward the cytosol in digitonin-permeabilized BY-2 cells (Figure S4C). Collectively, these results suggest that the recruitment of the GPAT8 1-92 mutant protein to ER subdomains by DGAT2 reflects a biologically relevant process. This conclusion is supported by other studies demonstrating that protein–protein interaction domains often exhibit the same protein-binding patterns regardless of whether they are expressed as single functional modules or within the context of the full-length proteins (71).

To identify the specific region within the GPAT8 1-92 construct that was responsible for interacting with DGAT2 and recruitment to DGAT2-enriched subdomains, we substituted each half of the predicted hydrophobic region in this construct (i.e. residues 50–89) with a hydrophobic sequence from another membrane protein (i.e. the first predicted TMD of DGAT1) and evaluated protein–protein interactions and subcellular targeting. These studies revealed that the second half of the hydrophobic region could be replaced without significantly altering protein–protein interactions or subdomain recruitment by DGAT2, but replacement of the first half essentially

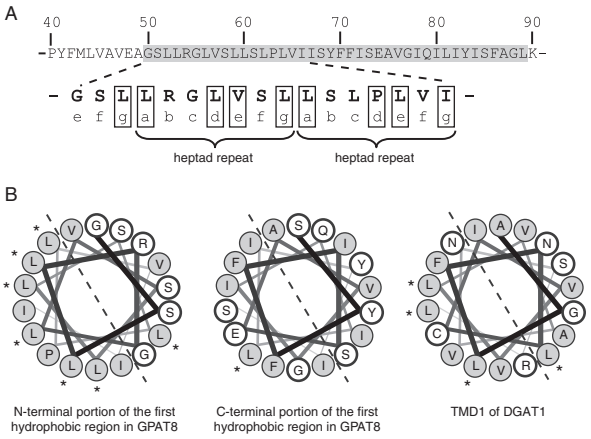

Figure 9: The polypeptide sequence corresponding to the first half of the N-terminal hydrophobic region of GPAT8 has propensity to form an amphipathic α-helix. A) Polypeptide sequence of GPAT8, with the numbers shown above representing the relative position of the amino acid residues in full-length GPAT8 and the first putative hydrophobic region (residues 50–89) highlighted in gray. The sequence representing the first half of the hydrophobic region shown to be important for interaction with DGAT2 and recruitment to ER subdomains by co-expression with DGAT2 (Figure 8) is expanded and highlighted in bold. Amino acids forming a hydrophobic heptad repeat (*abcdefg*) sequence, with leucine or other hydrophobic residues at positions *a*, *d*, *e* and *g*, are boxed. This motif matches the 'leucine-zipper' protein interaction motif described in several other membrane proteins (27,28). B) Helical wheel diagrams illustrating the formation of an amphipathic helix by the N-terminal, leucine-zipper-containing portion of the first hydrophobic region in GPAT8 (residues 50–67, left panel) and the lack of formation of an amphipathic helix by the C-terminal portion (residues 68–85, middle panel). Hydrophobic residues are shaded gray and hydrophilic residues are white. Leucine residues are marked with an asterisk. The helical wheel diagram for TMD1 derived from DGAT1, which was used to replace the N- and C-terminal portions of the first hydrophobic region in various mutant proteins (Figure 8), is shown in the right panel. Helical wheels were generated using an online algorithm available at http://cti.itc.virginia.edu/~cmg/Demo/wheel/wheelApp.html.

abolished both of these characteristics (Figure 8). Interestingly, by comparing the sequence and physicochemical properties of the N- and C-terminal portions of this hydrophobic region, potential insights to the protein targeting/interaction signal could be discerned (Figure 9). For instance, as shown in Figure 9B (left panel), the first half of the hydrophobic sequence forms an amphipathic α-helix when plotted on a helical wheel diagram. This property is not found in the second half of the sequence (Figure 9B, middle panel), despite having a similar overall level of hydrophobicity. Moreover, the sequence used to replace the hydrophobic portions of GPAT8 (i.e. DGAT1 TMD1) is also unable to form an amphipathic α-helix (Figure 9B, right panel), suggesting that an amphipathic helix serves as an important determinant in either the interaction of GPAT8 with DGAT2 and/or the trafficking of GPAT8 to ER subdomains. Additional support for this conclusion, albeit indirect, is that amphipathic helices are often involved in the trafficking of both cytosolic and membrane-bound proteins to specific locations in the cell. For instance, an amphipathic helix in β-arrestin is known to be important for recruitment of this soluble protein to activated, membrane-bound G protein-coupled receptors (72) and an amphipathic helix in the integral membrane protein Ist2 in yeast cells is important for the targeting and localization of the protein to ER subdomains that serve as contact sites with the plasma membrane (73).

Based on these and other examples, at least two potential scenarios can be envisioned that describe the interaction between GPAT8 and DGAT2. In one, the amphipathic helix in the first hydrophobic region of GPAT8 is located primarily in the cytosol or peripherally associated (rather than integrally) with ER membranes and interacts with a similar cytosol-exposed region(s) of DGAT2 to facilitate protein–protein interaction(s). In the second, the interaction of GPAT8 with DGAT2 results in burial of the GPAT8 amphipathic helix in the membrane, thereby adopting a more traditional TMD conformation and allowing the two proteins to be stabilized through helix–helix interactions. Notably, the amino sequence of the putative amphipathic helix in GPAT8 contains multiple repeats of a heptad (*abcdefg*) sequence enriched in leucine residues (Figure 9A), which is capable of forming a so-called leucine-zipper-like motif, a motif well known to mediate TMD-dependent protein–protein interactions of several other membrane-associated proteins (27,28). Of course, discriminating between these two (or other) scenarios will require identification of the specific region(s) of DGAT2 that are involved in interaction with GPAT8 and determining whether both of these regions (in GPAT8 and DGAT2) are located peripherally or integrally within the ER membrane, and also whether these topologies change upon their interaction and/or localization within their shared ER subdomains.

It is also worthwhile mentioning that amphipathic helices have the capacity to bind to certain types of lipids (as well as detect or induce membrane curvature), and that association of the helix with membranes can also result in activation of enzyme activity, a property known as amphitropism (26,73,74). Although it is presently unknown whether the amphipathic helix of GPAT8 might also be involved in sensing certain types of lipids, it is plausible that such a mechanism might exist to help the GPAT8 enzyme discriminate between various functional centers dedicated to synthesis of glycerolipids destined for cell membranes, storage oils or the cuticle. Furthermore, the activity of enzymes such as GPAT and DGAT will undoubtedly influence the local concentrations of lipid metabolites, thereby altering the physicochemical properties of the ER membranes themselves. These changes may further influence subdomain protein composition by reducing the thermodynamic capacity of resident proteins to remain in the local environment (thereby serving as a negative

feedback mechanism to reduce metabolic activity, similar to that observed for other enzymes, most notably cytidine 5′-triphosphate:phosphocholine cytidylyltransferase (75)). Alternatively, they can serve to attract additional protein components (e.g. other acyltransferases) that might help to maintain and/or increase the flux of metabolites through the pathway. We are currently testing this model by examining the ability of purified GPAT8, as well as peptide 'mimetics' (76,77) of the GPAT8 amphipathic sequence, to bind to various lipid compositions present in synthetic microsomal membranes.

Materials and Methods

Recombinant DNA procedures and reagents

Standard recombinant DNA procedures were performed as described by Sambrook et al. (78). Molecular biology reagents were purchased either from New England BioLabs, Promega, Perkin-Elmer Biosystems, Stratagene or Invitrogen. Oligonucleotides were synthesized by Invitrogen or Sigma-Genosys Canada. DNA was isolated and purified using reagents from Qiagen or Promega. All DNA constructs were verified using dye-terminated cycle sequencing performed at the Arizona State University DNA Laboratory, Mid-South Area Genomics Facility or the University of Guelph Genomics Facility. Mutagenesis was carried out using appropriate complementary forward and reverse mutagenic primers and the QuickChange site-directed mutagenesis kit according to the manufacturer's instructions (Stratagene). Complete details on all oligonucleotide primers used in the gene cloning and plasmid construction procedures (see below and *Materials and Methods* in Supporting Information) are provided in Table S1.

Tung GPAT8 and GPAT9 gene identification and sequence homology analysis

The gene encoding tung GPAT8 was initially identified by EST analysis of mRNA isolated from developing tung seeds (J.M. Shockey, unpublished data). The full-length gene was identified by adaptor-anchored polymerase chain reactions (PCRs) and the Universal GenomeWalker kit (Clontech) using gene-specific primers (Table S1) and tung genomic DNA as template. The putative translation initiation (ATG) codon in GPAT8 was then identified by DNA sequence alignments with other plant candidate GPAT8 genes available in public databases. Thereafter, gene-specific primers were used to amplify the full-length GPAT8 open reading frame (ORF) from developing tung seed first-strand cDNA using Pfu Ultra DNA polymerase (Stratagene). The resulting PCR products were A-tailed and then cloned into pCR2.1Topo (Invitrogen), yielding pCR2.1/GPAT8.

The amino acid sequences of plant-specific GPAT9 proteins are relatively well conserved (30), especially in the predicted phospholipid acyltransferase domain (refer Figure S2; blue-boxed region). We therefore isolated the corresponding region of tung GPAT9 genomic DNA by using degenerate PCR with the appropriate forward and reverse primers (Table S1). The resulting sequence was then used to isolate the remaining 5′ and 3′ portions of GPAT9 cDNA and gene by 5′ and 3′ rapid amplification of cDNA ends and genomic adaptor-anchored PCR, respectively. Plasmid pH17, containing the full-length GPAT9 ORF, was subsequently generated by restriction digest of the full-length GPAT9 ORF PCR product with *Bgl*II and *Pst*I, followed by ligation of the corresponding sites into pBEVY-L (79).

All known or predicted GPAT-like sequences described in this study were compared using the BLAST algorithm (80). Protein sequence alignments were conducted using the CLUSTALX program (81) using the default gap creation and gap extension penalty scores. Phylogenetic trees were drawn from the alignments using the TREEVIEW program (82). Bootstrap values were generated using the neighbor-joining method of Saitou and Nei (83), performing 1000 bootstrap trials, and a random number generator seed of 111.

Plasmid construction

A complete description of the construction of all plasmids used in this study is provided in the *Materials and Methods* of Supporting Information.

Biolistic bombardment and fluorescence microscopy

Tobacco (*Nicotiana tabacum* cv BY-2) suspension cell cultures were maintained and prepared for biolistic bombardment as described previously (84). Transient transformations were performed using 4 μg of plasmid DNA (or 2.5 μg of each plasmid for co-transformations) with a biolistic particle delivery system-1000/He (Bio-Rad Laboratories). Bombarded cells were incubated for approximately 4 h to allow for the expression and sorting of the introduced gene product(s), then either viewed immediately (via CLSM or epifluorescence microscopy, see below) or fixed in formaldehyde and incubated with 0.01% (w/v) pectolyase Y-23 (Kyowa Chemical Products), unless otherwise indicated. Thereafter, fixed cells were permeabilized with either 0.3% (v/v) Triton-X-100 or, for differential permeabilization experiments (refer Figures 6 and S4) 25 μg/mL digitonin (Sigma-Aldrich Ltd.) (58). Cells were evaluated for 4 h after biolistic bombardment to ensure that any potential negative effects because of (membrane) protein over-expression were diminished. In all experiments, at least 50 independently transformed cells were evaluated to determine subcellular localization of transiently (co-)expressed proteins, and all micrographs shown in the figures are representative images. Each experiment was replicated at least two times. Antibodies and sources were as follows: mouse anti-Myc antibodies in hybridoma medium (clone 9E10, Princeton University, Monoclonal Antibody Facility); rabbit anti-castor bean calreticulin (85); mouse anti-α-tubulin (Sigma-Aldrich Ltd.); rabbit anti-Myc (Bethyl Laboratories); mouse anti-HA (Covance); goat anti-mouse and goat anti-rabbit Alexa Fluor 488 IgGs, goat anti-mouse and goat anti-rabbit Cy5 (Cedar Lane Laboratories) and goat anti-rabbit rhodamine red-X IgGs (Jackson ImmunoResearch Laboratories). Con A conjugated to Alexa 594 (Molecular Probes) was added to cells at a final concentration of 5 μg/mL during the final 20 min of incubation with secondary antibodies.

CLSM images of BY-2 cells were acquired using a Leica DM RBE microscope with a Leica 63× Plan Apochromat oil-immersion objective, a Leica TCS SP2 scanning head and the LEICA TCS NT software package (Version 2.61) (Leica). Fluorophore emissions were collected sequentially in double- and triple-labeling experiments; single-labeling experiments showed no detectable crossover at the settings used for data collection. Confocal images were acquired as a z-series of representative cells and single optical sections were saved as 512 × 512-pixel digital images. Note that most CLSM images shown in this study are representative medial (mid-cell) optical sections of (co-)transformed cells, with the exception of those presented in Figure 2B,C, which show representative optical sections through the cell cortex. Note also that the extent to which fixed and living BY-2 cells were compressed by the coverslip during mounting (on glass slides) often influenced the amount of ER (membranes) that was observed in individual optical sections, i.e. depending on the compression of the cell by the coverslip, more or less of the ER network was observed in individual (medial) optical sections. Epifluorescent images of cells (refer Figures 6 and S4) were acquired using a Zeiss Axioscope 2 MOT epifluorescence microscope (Carl Zeiss, Inc.) with a Zeiss 63× Plan Apochromat oil-immersion objective. Image capture was performed using a Retiga 1300 charge-coupled device camera (Qimaging) and OPENLAB 5.0 software (Improvision). Figure compositions and merged images were generated using Adobe Photoshop CS and Illustrator CS2 (Adobe Systems).

The colocalization of proteins in selected CLSM optical sections was further quantified using the IMAGEJ plugin 'Colocalization Finder' (http://rsbweb.nih.gov/ij/plugins/colocalization-finder.html), and methods based on those described in (86,87). Briefly, regions-of-interest within the images of at least three separately (co-)transformed cells were split into

their individual red and green channels, then the corresponding pixels from the two channels were compared to calculate the Pearson's correlation coefficient *r*, which was expressed as mean ± standard deviation. *r* Values of −1.0 to 1.0 are considered to be equivalent to all of the pixels from the two corresponding channels being 100% non-colocalized to 100% colocalized, respectively. To obtain the colocalization mask, the colocalization plugin macro for IMAGEJ was used. Pixels were marked as colocalized if the signal was above a set threshold of 100 (range 0–255) and if their intensity ratio was higher than the ratio setting of 50%.

In vitro *membrane insertion experiments*

Preparation of salt-extracted canine pancreatic ER membranes (microsomes), transcription reactions using SP6 polymerase (MBI Fermentas, Inc.) and rabbit reticulocyte lysate-directed protein translations using 35S-methionine (Perkin-Elmer Biosystems-NEN) in the presence or absence of microsomes was carried out as previously described ((88) and references therein). For post-translational insertion assays, microsomes were added to cycloheximide-terminated translation reactions and incubated for 1 h at 24°C. All reactions had a final volume of 11 μL. An equal volume of buffer (4 M urea, 1 mM DTT, 50 mM KCl, 2.5 mM $MgCl_2$, 10 mM Tris–HCl, pH 7.5) was then added to each reaction and both co- and post-translation reactions were layered onto a 44 μL sucrose cushion (2 M urea, 0.5 M sucrose, 1 mM DTT, 50 mM KCl, 2.5 mM $MgCl_2$, 10 mM Tris–HCl, pH. 7.5) and centrifuged at 100 000 × ***g*** for 15 min at 4°C using a TL-100 ultracentrifuge and TLA100 rotor (Beckman). The sample was then divided into three fractions, representing the top (T, ×33 μL), middle (M, ×33 μL) and bottom (B) fractions (consisting of the microsome-containing pellet resuspended in 63 μL of SDS–PAGE loading buffer). Top and middle fractions were also diluted in (30 μL) SDS–PAGE loading buffer. An equivalent percentage volume of each fraction was then analyzed by SDS–PAGE. Labeled proteins were visualized using BioFlex MRI Single-Emulsion X-Ray Film (Clonex), followed by X-ray development and digital scanning.

Membrane integration was determined by washing pelleted microsomes with alkaline sodium carbonate, as previously described (89). Briefly, membranes collected in the bottom fraction (see above) were resuspended in 0.1 mM Na_2CO_3 (pH 11.5) and after 30 min at 0°C the sample was layered onto a 0.5 M sucrose cushion and centrifuged at 100 000 × ***g*** for 10 min. Integral membrane proteins in the pellet fraction (P) and soluble (lumenal) and peripheral membrane proteins in the supernatant (S) were collected and analyzed by SDS–PAGE as above.

Split-ub-based membrane yeast two-hybrid assay

The DUALmembrane split-Ub system (Dualsystems Biotech) was used as described in the manufacturer's instructions, with some modifications. Briefly, yeast cells (strain NMY51) harboring bait and prey plasmids were cultured overnight in 3 mL synthetic dextrose medium [2% (w/v) dextrose, 0.67% (w/v) yeast nitrogen base without amino acids, 2 g/L synthetic mix of amino acid supplements, minus leucine and tryptophan; SD-LT] (Bufferad) in an orbital shaker at 30°C and 300 rotations/min. The following day, 500 μL of cell culture was transferred to 10 mL of fresh SD-LT medium and the cells were cultured as above for another 3.5 h. Cells were pelleted by centrifugation, washed once with water, then resuspended in 1 mL of water. To test for activation of the HIS and ADE reporter genes, a serial dilution assay was performed where the first cell suspension had an OD_{600} value of 0.5, and six subsequent samples were prepared by 1:5 serial dilution. Cells from each sample were plated on SD-LT and SD-LTHA plates (SD-LT medium that also lacked histidine and adenine) and incubated for 2 days at 30°C. Activation of the lacZ reporter in the yeast strain was evaluated by spotting yeast cells in duplicate (from the 0.5 OD_{600} sample) onto SD-LT plates containing 80 μg/mL X-Gal (5-bromo-4-chloro-3-indolyl-β-D-galactopyranoside) or by quantitative analysis of β-gal activity using the β-gal assay kit from Pierce Protein Research Products (Thermo Scientific). Enzyme activity was calculated in Miller Units (90) and was normalized based on the relative amount of prey proteins (determined by quantitative western blotting using the HA-epitope tag present on each Nub-fusion protein; see Figure 4). Specifically, protein normalization factors were determined by densitometry of a representative western blot and comparison of Nub-fusion protein amounts to the positive control protein Alg5-NubI. Each set of bait and prey yeast strains used in this study was evaluated by similar quantitative anti-HA western blotting techniques, and revealed that the relative amounts of Nub-fusion proteins were similar, regardless of the various bait proteins used (data not shown). Whole cell lysates were prepared and analyzed by SDS–PAGE and western blotting as described by O'Quin et al. (91). Digital imaging and densitometry were performed using chemiluminescence substrates and a Fuji LAS-4000 imaging system (Fujifilm Medical Systems).

Sequence data from this article can be found in the following references and Genbank/EMBL data library: *Arabidopsis* GPAT1 through GPAT7 (32); tung GPAT8 (FJ479753, HM461980) and GPAT9 (FJ479751, HM461981); *Arabidopsis* GPAT8 (BT015813; (34)) and GPAT9 (FJ479752; (30)); *Escherichia coli* GPAT (K00127.1; (92)); *Saccharomyces cerevisiae* GAT1 (AJ311354.1) and GAT2 (AJ314608.1; (93)); *Mus musculus* GPAT1 (AAA37647; (94)), GPAT2 (BAD21404; (95)), GPAT3 (NM_172715; (36)); GPAT4 (NM_018743; (96)); castor GPAT8 (XP_002511873.1) and GPAT9 (ACB30546.1); poplar GPAT8 (XP_002320138.1) and GPAT9 (XP_002305552.1); grape GPAT8 (XP_002275348.1) and GPAT9 (CAN62196.1); and soybean GPAT9 (ACU2375 7.1).

Acknowledgments

The authors gratefully acknowledge O. Guerra Peraza for assistance with plasmid constructions, Stephen Vinyard and Philip Loftis for help with the split-Ub analysis and Federica Brandizzi for providing the plasmid pVKH18En6-Sec24. The authors also thank the anonymous referees for their constructive comments that led to an improved version of the article. This work was supported by a grant from the Natural Sciences and Engineering Research Council of Canada (NSERC grant no. 217291) to R. T. M., the United States Department of Agriculture, Current Research Information System (CRIS) project number 5347-21000-005-00D to J. M. D., CRIS project no. 6435-41000-087-00D to J. M. S. and the Canadian Institutes of Health Research (FRN 10490) to D. W. A. D. W. A. holds a Canada Research Chair in Membrane Biogenesis and R. T. M. holds a University of Guelph Research Chair. Financial support for S. K. G. was provided by funds from the Ontario Research and Development Challenge Fund (Ontario Centre for Agricultural Genomics) (grant no. 046061) to S. J. R.

Supporting Information

Additional Supporting Information may be found in the online version of this article:

Figure S1: Alignment of GPAT8-like protein sequences. Putative GPAT8 homologs were identified using BLASTP (http://blast.ncbi.nlm.nih.gov/Blast.cgi) and the tung GPAT8 sequence as a query. Protein sequences were aligned using the CLUSTALW algorithm (http://npsa-pbil.ibcp.fr/cgi-bin/npsa_automat.pl?page=npsa_clustalw.html) (81) and share 70% identity, 89% similarity over their entire polypeptide length. The proteins contain two hydrophobic regions (orange boxes) that are predicted, based on TMPRED (http://www.ch.embnet.org/software/TMPRED_form/html), TOPCONS (http://topcons.cbr.su.se/), TMHMM (http://www.cbs.dtu.dk/servides/TMHMM/) and visual inspection of the sequences to contain one or more membrane-spanning α-helices. The first region includes a stretch of approximately 40 amino acids beginning around position 50 and the second stretch includes approximately 23 amino acids near position 250. A putative proline knot motif (-LPF-) in the second hydrophobic region is highlighted in bold. The blue-boxed region corresponds to a phospholipid acyltransferase domain in tung GPAT8 identified using the InterProScan algorithm (http://www.ebi.ac.uk/Tools/InterProScan/) and putative C-terminal dilysine motifs (30) are highlighted in gray. Residues known to be important for

substrate binding and acyltransferase activity (97) are marked by down arrows.

Figure S2: Alignment of GPAT9-like protein sequences. Putative GPAT9 homologs were identified using BLASTP and the tung GPAT9 sequence as a query. Protein sequences were aligned using the CLUSTALW algorithm and share 77% identity, 90% similarity over their entire polypeptide length. Hydrophobic regions predicted to form a transmembrane helical segment (orange boxes) were identified using TMPRED, TOPCONS, TMHMM and visual inspection of the sequences. The blue-boxed region corresponds to a phospholipid acyltransferase domain in tung GPAT9 identified using the InterProScan algorithm, and putative C-terminal ER retrieval motifs (30) are highlighted in gray. Residues known to be important for substrate binding and acyltransferase activity (97) are marked by down arrows.

Figure S3: Subcellular localization of GPAT8, GPAT9, Cb5 or Sec24 in fixed and/or living BY-2 cells. Representative micrographs of BY-2 cells transiently (co-)transformed with GFP-tagged versions of GPAT8 or GPAT9 (A), Cb5 (B) or Sec24 (C) and RFP-ER and viewed using CLSM. Cells were viewed under either living or formaldehyde-fixed conditions (as indicated on each row of panels). Shown are representative optical z-sections of (co-)transformed cells at the cell median. Hatched boxes represent the portion of the cell shown at higher magnification in the panels to the right. The yellow/orange color in the merged images indicates colocalizations of co-expressed proteins in the same cells; white arrows indicate obvious localizations of co-expressed GFP fusion protein and RFP-ER in distinct regions of the ER. Bar = 10 μm.

Figure S4: Topological mapping of CBR and the GPAT8 1-92 mutant in differential detergent-permeabilized BY-2 cells. Representative micrographs of BY-2 cells either transiently transformed with N- or C-terminal-appended Myc-tagged-versions of tung CBR (A), non-transformed (B) or transiently (co-)transformed with Myc-GPAT8 1-92 expressed on its own or co-expressed with full-length HA-DGAT2 (C). Cells were fixed in formaldehyde at approximately 4 h after biolistic bombardment, permeabilized using either digitonin, which selectively permeabilizes the plasma membrane or Triton-X-100, which permeabilizes all cellular membranes (58), and then processed for (immuno)epifluorescence microscopy. Each micrograph is labeled at the top left with the name of either the (co-)expressed epitope-tagged protein or the corresponding endogenous marker protein (i.e. ER-lumenal calreticulin or cytosolic α-tubulin), as well as the detergent (Triton-X-100 or digitonin) used to permeabilize these cells. Also shown for each set of immunostained cells is the corresponding differential interference contrast (DIC) image. Note in (C) that Myc-GPAT8 1-92 either expressed on its own and localized to the cytosol (left three panels) or co-expressed with HA-DGAT2 and localized to ER subdomains (right three panels) was immunodetectable, whereas endogenous calreticulin in the same digitonin-permeabilized cells was not. Note also in (C) that the immunostaining attributable to co-expressed HA-DGAT2 in ER subdomains is not shown. Bar = 10 μm.

Table S1: List of synthetic oligonucleotide primers used in the isolation of tung *GPAT* genes and the construction of plasmids (see *Materials and Methods*; 98, 99)

Please note: Wiley-Blackwell are not responsible for the content or functionality of any supporting materials supplied by the authors. Any queries (other than missing material) should be directed to the corresponding author for the article.

References

1. Lindner R, Naim HY. Domains in biological membranes. Exp Cell Res 2009;315:2871–2878.
2. Dekker JP, Boekema EJ. Supramolecular organization of thylakoid membrane proteins in green plants. Biochim Biophys Acta 2005;1706:12–39.
3. Lenaz G, Genova ML. Structural and functional organization of the mitochondrial respiratory chain: a dynamic super-assembly. Int J Biochem Cell Biol 2009;41:1750–1772.
4. Hanson MR, Sattarzadeh A. Dynamic morphology of plastids and stromules in angiosperm plants. Plant Cell Environ 2008;31:646–657.
5. Logan DC. Plant mitochondrial dynamics. Biochim Biophys Acta 2006;1763:430–441.
6. Scott I, Sparkes IA, Logan DC. The missing link: inter-organellar connections in mitochondria and peroxisomes? Trends Plant Sci 2007;12:380–381.
7. Borgese N, Francolini M, Snapp E. Endoplasmic reticulum architecture: structures in flux. Curr Opin Cell Biol 2006;18:358–364.
8. English AR, Nesia Zurek N, Voeltz GK. Peripheral ER structure to function. Curr Opin Cell Biol 2009;21:596–602.
9. Levine T, Rabouille C. Endoplasmic reticulum: one continuous network compartmentalized by extrinsic cues. Curr Opin Cell Biol 2005;17:362–368.
10. Sparkes IA, Frigerio L, Tolley N, Hawes C. The plant endoplasmic reticulum: a cell-wide web. Biochem J 2009;423:145–155.
11. Staehelin LA. The plant ER: a dynamic organelle composed of a large number of discrete functional domains. Plant J 1997;11:1151–1165.
12. Voeltz GK, Rolls MM, Rapoport TA. Structural organization of the endoplasmic reticulum. EMBO Rep 2002;3:944–950.
13. Budnik A, Stephens DJ. ER exit sites – localization and control of COPII vesicle formation. FEBS Lett 2009;583:3796–3803.
14. Marti L, Fornaciari S, Renna L, Stefano G, Brandizzi F. COPII-mediated traffic in plants. Trends Plant Sci 2010;15:522–528.
15. Mullen RT, Trelease RN. The ER-peroxisome connection in plants: development of the ''ER semi-autonomous peroxisome maturation and replication'' model for plant peroxisome biogenesis. Biochim Biophys Acta 2006;1763:1655–1668.
16. Crofts AJ, Washida H, Okita TW, Satoh M, Ogawa M, Kumamaru T, Satoh H. The role of mRNA and protein sorting in seed storage protein synthesis, transport, and deposition. Biochem Cell Biol 2005;83:728–737.
17. Listenberger LL, Brown DA. Lipid droplets. Curr Biol 2008;18: R237–R238.
18. Murphy DJ. The biogenesis and functions of lipid bodies in animals, plants and microorganisms. Prog Lipid Res 2001;40:325–438.
19. Robenek H, Buers I, Hofnagel O, Robenek MJ, Troyer D, Severs NJ. Compartmentalization of proteins in lipid droplet biogenesis. Biochim Biophys Acta 2009;1791:408–418.
20. Robenek H, Hofnagel O, Buers I, Robenek MJ, Troyer D, Severs NJ. Adipophilin-enriched domains in the ER membrane are sites of lipid droplet biogenesis. J Cell Sci 2006;119:4215–4224.
21. Pol A, Martin S, Fernandez MA, Ferguson C, Carozzi A, Luetterforst R, Enrich C, Parton RG. Dynamic and regulated association of caveolin with lipid bodies: modulation of lipid body motility and function by a dominant negative mutant. Mol Biol Cell 2004;15:99–110.
22. Turró S, Ingelmo-Torres M, Estanyol JM, Tebar F, Fernández MA, Albor CV, Gaus K, Grewal T, Enrich C, Pol A. Identification and characterization of associated with lipid droplet protein 1: a novel membrane-associated protein that resides on hepatic lipid droplets. Traffic 2006;7:1254–1269.
23. Shockey JM, Gidda SK, Chapital DC, Kuan JC, Dhanoa PK, Bland JM, Rothstein SJ, Mullen RT, Dyer JM. Tung tree DGAT1 and DGAT2 have nonredundant functions in triacylglycerol biosynthesis and are localized to different subdomains of the endoplasmic reticulum. Plant Cell 2006;18:2294–2313.
24. Heinzer S, Wörz S, Kalla C, Rohr K, Weiss M. A model for the self-organization of exit sites in the endoplasmic reticulum. J Cell Sci 2008;121:55–64.
25. Szczesna-Skorupa E, Kemper B. Influence of protein–protein interactions on the cellular localization of cytochrome P450. Expert Opin Drug Metab Toxicol 2008;4:123–136.
26. Cornell RB, Taneva S. Amphipathic helices as mediators of the membrane interaction of amphitropic proteins, and as modulators of bilayer physical properties. Curr Protein Pept Sci 2006;7:539–552.
27. Gurezka R, Laage R, Brosig B, Langosch D. A heptad motif of leucine residues found in membrane proteins can drive self-assembly of artificial transmembrane segments. J Biol Chem 1999;274:9265–9270.
28. Moore DT, Berger BW, DeGrado WF. Protein–protein interactions in the membrane: sequence, structural, and biological motifs. Structure 2008;16:991–1001.

29. Dyer JM, Mullen RT. Engineering plant oils as high-value industrial feedstocks for biorefining: the need for underpinning cell biology research. Physiol Plant 2008;132:11–22.
30. Gidda SK, Shockey JM, Rothstein SJ, Dyer JM, Mullen RT. *Arabidopsis thaliana* GPAT8 and GPAT9 are localized to the ER and possess distinct ER retrieval signals: functional divergence of the dilysine ER retrieval motif in plant cells. Plant Physiol Biochem 2009;47:867–879.
31. Ohlrogge J, Browse J. Lipid biosynthesis. Plant Cell 1995;7:957–970.
32. Zheng Z, Xia Q, Daux M, Shen W, Selvaraj G, Zou J. *Arabidopsis* AtGPAT1, a member of the membrane-bound glycerol-3-phosphate acyltransferase gene family, is essential to tapetum differentiation and male fertility. Plant Cell 2003;15:1872–1887.
33. Beisson F, Li Y, Bonaventure G, Pollard M, Ohlrogge JB. The acyltransferase GPAT5 is required for the synthesis of suberin in seed coat and root of *Arabidopsis*. Plant Cell 2007;19:351–368.
34. Li Y, Beisson F, Koo AJK, Molina I, Pollard M, Ohlrogge J. Identification of acyltransferases required for cutin biosynthesis and production of cutin with suberin-like monomers. Proc Natl Acad Sci U S A 2007;104:18339–18344.
35. Yang W, Pollard M, Li-Beisson Y, Beisson F, Feig M, Ohlrogge J. A distinct type of glycerol-3-phosphate acyltransferase with sn-2 preference and phosphatase activity producing 2-monoacylglycerol. Proc Natl Acad Sci U S A 2010;107:12040–12045.
36. Cao J, Li J-L, Li D, Tobin JF, Gimeno RE. Molecular identification of microsomal acyl-CoA:glycerol-3-phosphate acyltransferase, a key enzyme in *de novo* triacylglycerol synthesis. Proc Natl Acad Sci U S A 2006;103:19695–19700.
37. Brandizzi F, Irons S, Kearns A, Hawes C. BY-2 cells: culture and transformation for live cell imaging. Curr Protoc Cell Biol 2003;1.7:1–16.
38. Miao Y, Jiang LW. Transient expression of fluorescent fusion proteins in protoplasts of suspension cultured cells. Nat Protoc 2007;2:2348–2353.
39. Tartakoff AM, Vassalli P. Lectin-binding sites as markers of Golgi subcompartments: proximal-to-distal maturation of oligosaccharides. J Cell Biol 1983;97:1243–1248.
40. Griffing LR. Networking in the endoplasmic reticulum. Biochem Soc Trans 2009;38:747–753.
41. Hwang YT, Pelitire SM, Henderson MPA, Andrews DW, Dyer JM, Mullen RT. Novel targeting signals mediate the sorting of different isoforms of the tail-anchored membrane protein cytochrome b5 to either endoplasmic reticulum or mitochondria. Plant Cell 2004;16:3002–3019.
42. Hanton SL, Matheson LA, Chatre L, Brandizzi F. Dynamic organization of COPII coat proteins at endoplasmic reticulum export sites in plant cells. Plant J 2009;57:963–974.
43. Mersey B, McCully ME. Monitoring the course of fixation in plant cells. J Microsc 1978;114:49–76.
44. Kiss JZ, Giddings TH Jr, Staehelin LA, Sack FD. Comparison of the ultrastructure of conventionally fixed and high pressure frozen/freeze substituted root tips of *Nicotiana* and *Arabidopsis*. Protoplasma 1990;157:64–74.
45. Zechmann B, Müller M, Zellnig G. Membrane associated qualitative differences in cell ultrastructure of chemically and high pressure cryofixed plant cells. J Struct Biol 2007;158:370–377.
46. Moore I, Murphy A. Validating the localization of fluorescent protein fusions in the endomembrane system. Plant Cell 2009;21:1632–1636.
47. Nziengui H, Schoefs B. Functions of reticulons in plants: what we can learn from animals and yeasts. Cell Mol Life Sci 2009;66:584–595.
48. Yang YD, Elamawi R, Bubeck J, Pepperkok R, Ritzenthaler C, Robinson DG. Dynamics of COPII vesicles and the Golgi apparatus in cultured *Nicotiana tabacum* BY-2 cells provides evidence for transient association of Golgi stacks with endoplasmic reticulum exit sites. Plant Cell 2005;17:1513–1531.
49. Gupton SL, Collings DA, Allen NS. Endoplasmic reticulum targeted GFP reveals ER organization in tobacco NT-1 cells during cell division. Plant Physiol Biochem 2006;44:95–105.
50. Yokota E, Ueda S, Tamura K, Orii H, Uchi S, Sonobe S, Hara-Nishimura I, Shimmen T. An isoform of myosin XI is responsible for the translocation of endoplasmic reticulum in tobacco cultured BY-2 cells. J Exp Bot 2009;60:197–212.
51. Sparkes I, Tolley N, Aller I, Svozil J, Osterrieder A, Botchway S, Mueller C, Frigerio L, Hawes C. Five *Arabidopsis* reticulon isoforms share endoplasmic reticulum location, topology, and membrane-spanning properties. Plant Cell 2010;22:1333–1343.
52. Ueda H, Yokota E, Kutsuna N, Shimada T, Tamura K, Shimmen T, Hasezawa S, Dolja VV, Hara-Nishimura I. Myosin-dependent endoplasmic reticulum motility and F-actin organization in plant cells. Proc Natl Acad Sci U S A 2010;107:6894–6899.
53. Snider J, Kittanakom S, Curak J, Stagljar I. Split-ubiquitin based membrane yeast two-hybrid (MYTH) system: a powerful tool for identifying protein–protein interactions. J Vis Exp 2010;36:1698.
54. Deslandes L, Olivier J, Peeters N, Feng DX, Khounlotham M, Boucher C, Somssich I, Genin S, Marco Y. Physical interaction between RRS1-R, a protein conferring resistance to bacterial wilt, and PopP2, a type III effector targeted to the plant nucleus. Proc Natl Acad Sci U S A 2003;100:8024–8029.
55. Obrdlik P, El-Bakkoury M, Hamacher T, Cappellaro C, Vilarino C, Fleischer C, Ellerbrok H, Kamuzinzi R, Ledent V, Blaudez D, Sanders D, Revuelta JL, Boles E, Andre B, Frommer WB. K+ channel interactions detected by a genetic system optimized for systematic studies of membrane protein interactions. Proc Natl Acad Sci U S A 2004;101:12242–12247.
56. Johnsson N, Varshavsky A. Split ubiquitin as a sensor of protein interactions *in vivo*. Proc Natl Acad Sci U S A 1994;91:10340–10344.
57. Heesen S, Lehle L, Weissmann A, Aebi M. Isolation of the ALG5 locus encoding the UDP-glucose:dolichyl-phosphate glucosyltransferase from *Saccharomyces cerevisiae*. Eur J Biochem 1994;224:71–79.
58. Lee MS, Mullen RT, Trelease RN. Oilseed isocitrate lyases lacking their essential type-1 peroxisomal targeting signal are piggybacked to glyoxysomes. Plant Cell 1997;9:185–197.
59. Shockey JM, Dhanoa PK, Dupuy T, Chapital DC, Mullen RT, Dyer JM. Cloning, functional analysis, and subcellular localization of two isoforms of NADH:cytochrome b_5 reductase from developing seeds of tung (*Vernicia fordii*). Plant Sci 2005;169:375–385.
60. Janiak F, Glover JR, Leber B, Rachubinski RA, Andrews DW. Targeting of passenger proteins to multiple intracellular membranes. Biochem J 1994;300:191–199.
61. Kim PK, Janiak-Spens F, Trimble WS, Leber B, Andrews DW. Evidence for multiple mechanisms for membrane binding and integration via carboxyl-terminal insertion sequences. Biochemistry 1997;36:8873–8882.
62. Cordes FS, Bright JN, Sansom MS. Proline-induced distortions of transmembrane helices. J Mol Biol 2002;323:951–960.
63. Holt A, Killian JA. Orientation and dynamics of transmembrane peptides: the power of simple models. Eur Biophys J 2010;39:609–621.
64. Malbon CC, Tao J, Wang HY. AKAPs (A-kinase anchoring proteins) and molecules that compose their G-protein-coupled receptor signaling complexes. Biochem J 2004;379:1–9.
65. Weselake RJ, Madhavji M, Szarka SJ, Patterson NA, Wiehler WB, Nykiforuk CL, Burton TL, Boora PS, Mosimann SC, Foroud NA, Thibault BJ, Moloney MM, Laroche A, Furukawa-Stoffer TL. Acyl-CoA-binding and self-associating properties of a recombinant 13.3 kDa N-terminal fragment of diacylglycerol acyltransferase-1 from oilseed rape. BMC Biochem 2006;27:24.
66. McFie PJ, Stone SL, Banman SL, Stone SJ. Acyl CoA:diacylglycerol acyltransferase-1 (DGAT1): topological orientation, identification of a putative active site histidine and the role of the N-terminus in dimer/tetramer formation. J Biol Chem 2010;285:37377–37387.
67. Tolley N, Sparkes I, Craddock CP, Eastmond PJ, Runions J, Hawes C, Frigerio L. Transmembrane domain length is responsible for the ability of a plant reticulon to shape endoplasmic reticulum tubules *in vivo*. Plant J 2010;64:411–418.
68. Tolley N, Sparkes I, Hunter PR, Craddock CP, Nuttall J, Roberts LM, Hawes C, Pedrazzini E, Frigerio L. Overexpression of a plant reticulon remodels the lumen of the cortical endoplasmic reticulum but does not perturb protein transport. Traffic 2008;9:94–102.
69. Dyer JM, Chapital DC, Kuan JC, Mullen RT, Turner C, McKeon TA, Pepperman AB. Molecular analysis of a bifunctional fatty acid conjugase/desaturase from tung. Implications for the evolution of plant fatty acid diversity. Plant Physiol 2002;130:2027–2038.
70. Gimeno RE, Cao J. Mammalian glycerol-3-phosphate acyltransferases: new genes for an old activity. J Lipid Res 2008;49:2079–2088.
71. Boxem M, Maliga Z, Klitgord N, Li N, Lemmens I, Mana M, de Lichtervelde L, Mul JD, van de Peut D, Devos M, Simonis N,

Yildirim MA, Cokol M, Kao HL, de Smet AS et al. A protein domain-based interactome network for *C. elegans* early embryogenesis. Cell 2008;134:534–545.
72. Vishnivetskiy SA, Francis D, Van Eps N, Kim M, Hanson SM, Klug CS, Hubbell WL, Gurevich VV. The role of arrestin alpha-helix I in receptor binding. J Mol Biol 2010;395:42–54.
73. Maass K, Fischer MA, Seiler M, Temmerman K, Nickel W, Seedorf M. A signal comprising a basic cluster and an amphipathic alpha-helix interacts with lipids and is required for the transport of Ist2 to the yeast cortical ER. J Cell Sci 2009;122:625–635.
74. Duncan RE, Wang Y, Ahmadian M, Lu J, Sarkadi-Nagy E, Sul HS. Characterization of desnutrin functional domains: critical residues for triacylglycerol hydrolysis in cultured cells. J Lipid Res 2010;51:309–317.
75. Cornell RB, Northwood IC. Regulation of CTP:phosphocholine cytidylyltransferase by amphitropism and relocalization. Trends Biochem Sci 2000;25:441–447.
76. Ross NT, Katt WP, Hamilton AD. Synthetic mimetics of protein secondary structure domains. Philos Transact A Math Phys Eng Sci 2010;368:989–1008.
77. Starovasnik MA, Braisted AC, Wells JA. Structural mimicry of a native protein by a minimized binding domain. Proc Natl Acad Sci U S A 1997;94:10080–10085.
78. Sambrook J, Fritsch EF, Maniatis T. Molecular Cloning: A Laboratory Manual, 2nd edn. Cold Spring Harbor, NY: Cold Spring Harbor Laboratory Press; 1989.
79. Millar CA, Martinat MA, Hyman LE. Assessment of aryl hydrocarbon receptor complex interactions using pBEVY plasmids: expression-vectors with bi-directional promoters for use in *Saccharomyces cerevisiae*. Nucleic Acids Res 1998;26:3577–3583.
80. Altschul SF, Madden TL, Schaffer AA, Zhang J, Zhang Z, Miller W, Lipman DJ. Gapped BLAST and PSI-BLAST: a new generation of protein database search programs. Nucleic Acids Res 1997;25: 3389–3402.
81. Thompson JD, Gibson TJ, Plewniak F, Jeanmougin F, Higgins DG. The CLUSTAL_X windows interface: flexible strategies for multiple sequence alignment aided by quality analysis tools. Nucleic Acids Res 1997;25:4876–4882.
82. Page RD. TreeView: an application to display phylogenetic trees on personal computers. Comput Appl Biosci 1996;12:357–358.
83. Saitou N, Nei M. The neighbor-joining method: a new method for reconstructing phylogenetic trees. Mol Biol Evol 1987;4:406–425.
84. Lingard MJ, Gidda SK, Bingham S, Rothstein SJ, Mullen RT, Trelease RN. *Arabidopsis* PEROXIN11c-e, FISSION1b, and DYNAMIN-RELATED PROTEIN3A cooperate in cell cycle-associated replication of peroxisomes. Plant Cell 2008;20:1567–1585.
85. Coughlan SJ, Hastings C, Winfrey R Jr. Cloning and characterization of the calreticulin gene from *Ricinus communis* L. Plant Mol Biol 1997;34:897–911.
86. French AP, Mills S, Swarup R, Bennett MJ, Pridmore TP. Colocalization of fluorescent markers in confocal images of plant cells. Nat Protoc 2008;3:619–628.
87. Barlow AL, Macleod A, Noppen S, Sanderson J, Guérin CJ. Colocalization analysis in fluorescence micrographs: verification of a more accurate calculation of Pearson's correlation coefficient. Microsc Microanal 2010;16:710–724.
88. McCartney AW, Dyer JM, Dhanoa PK, Kim PK, Andrews DW, McNew JA, Mullen RT. Membrane-bound fatty acid desaturases are inserted co-translationally into the ER and contain different ER retrieval motifs at their carboxy termini. Plant J 2004;37:156–173.
89. Andrews DW, Young JC, Mirels LF, Czarnota GJ. The role of the N region in signal sequence and signal-anchor function. J Biol Chem 1992;267:7761–7769.
90. Miller JF. Experiments in Molecular Genetics. Cold Spring Harbor, NY: Cold Spring Harbor Laboratory Press; 1972.
91. O'Quin JB, Bourassa L, Zhang D, Shockey JM, Gidda SK, Fosnot S, Chapman KD, Mullen RT, Dyer JM. Temperature-sensitive, post-translational regulation of plant omega-3 fatty acid desaturases is mediated by the ER-associated degradation pathway. J Biol Chem 2010;285:21781–21796.
92. Lightner VA, Larson TJ, Tailleur P, Kantor GD, Raetz CRH, Bell RM, Modrich P. Membrane phospholipid synthesis in *Escherichia coli*. Cloning of a structural gene (plsB) of the sn-glycerol-3-phosphate acyl/transferase. J Biol Chem 1980;255:9413–9420.
93. Zheng Z, Zou J. The initial step of the glycerolipid pathway. Identification of glycerol-3-phosphate/dihydroxyacetone phosphate dual substrate acyltransferases in *Saccharomyces cerevisiae*. J Biol Chem 2001;276:41710–41716.
94. Yet SF, Lee S, Hahm YT, Sul HS. Expression and identification of p90 as the murine mitochondrial glycerol-3-phosphate acyltransferase. Biochemistry 1993;32:9486–9491.
95. Lewin TM, Schwerbrock NM, Lee DP, Coleman RA. Identification of a new glycerol-3-phosphate acyltransferase isoenzyme, mtGPAT2, in mitochondria. J Biol Chem 2004;279:13488–13495.
96. Nagle CA, Vergnes L, Dejong H, Wang S, Lewin TM, Reue K, Coleman RA. Identification of a novel sn-glycerol-3-phosphate acyltransferase isoform, GPAT4, as the enzyme deficient in Agpat62/2 mice. J Lipid Res 2008;49:823–831.
97. Lewin TM, Wang P, Coleman RA. Analysis of amino acid motifs diagnostic for the sn-glycerol-3-phosphate acyltransferase reaction. Biochemistry 1999;38:5764–5771.
98. Fritze CE, Anderson TR. Epitope tagging: general method for tracking recombinant proteins. Methods Enzymol 2000;327:3–16.
99. Shaner NC, Campbell RE, Steinbach PA, Giepmans BN, Palmer AE, Tsien RY. Improved monomeric red, orange and yellow fluorescent proteins derived from *Discosoma* sp. red fluorescent protein. Nat Biotechnol 2004;22:1567–1572.

Figure S1: Alignment of GPAT8-like protein sequences. Putative GPAT8 homologs were identified using BLASTP (http://blast.ncbi.nlm.nih.gov/Blast.cgi) and the tung GPAT8 sequence as a query. Protein sequences were aligned using the CLUSTALW algorithm (http://npsa-pbil.ibcp.fr/cgi-bin/npsa_automat.pl?page=npsa_clustalw.html) (81) and share 70% identity, 89% similarity over their entire polypeptide length. The proteins contain two hydrophobic regions (orange boxes) that are predicted, based on TMPRED (http://www.ch.embnet.org/software/TMPRED_form/html), TOPCONS (http://topcons.cbr.su.se/), TMHMM (http://www.cbs.dtu.dk/servides/TMHMM/) and visual inspection of the sequences to contain one or more membrane-spanning α-helices. The first region includes a stretch of approximately 40 amino acids beginning around position 50 and the second stretch includes approximately 23 amino acids near position 250. A putative proline knot motif (-LPF-) in the second hydrophobic region is highlighted in bold. The blue-boxed region corresponds to a phospholipid acyltransferase domain in tung GPAT8 identified using the InterProScan algorithm (http://www.ebi.ac.uk/Tools/InterProScan/) and putative C-terminal dilysine motifs (30) are highlighted in gray. Residues known to be important for substrate binding and acyltransferase activity (97) are marked by down arrows.

Figure S2: Alignment of GPAT9-like protein sequences. Putative GPAT9 homologs were identified using BLASTP and the tung GPAT9 sequence as a query. Protein sequences were aligned using the CLUSTALW algorithm and share 77% identity, 90% similarity over their entire polypeptide length. Hydrophobic regions predicted to form a transmembrane helical segment (orange boxes) were identified using TMPRED, TOPCONS, TMHMM and visual inspection of the sequences. The blue-boxed region corresponds to a phospholipid acyltransferase domain in tung GPAT9 identified using the InterProScan algorithm, and putative C-terminal ER retrieval motifs (30) are highlighted in gray. Residues known to be important for substrate binding and acyltransferase activity (97) are marked by down arrows.

Figure S3: Subcellular localization of GPAT8, GPAT9, Cb5 or Sec24 in fixed and/or living BY-2 cells. Representative micrographs of BY-2 cells transiently (co-)transformed with GFP-tagged versions of GPAT8 or GPAT9 (A), Cb5 (B) or Sec24 (C) and RFP-ER and viewed using CLSM. Cells were viewed under either living or formaldehyde-fixed conditions (as indicated on each row of panels). Shown are representative optical z-sections of (co-)transformed cells at the cell median. Hatched boxes represent the portion of the cell shown at higher magnification in the panels to the right. The yellow/orange color in the merged images indicates colocalizations of co-expressed proteins in the same cells; white arrows indicate obvious localizations of co-expressed GFP fusion protein and RFP-ER in distinct regions of the ER. Bar = 10 µm.

Figure S4: Topological mapping of CBR and the GPAT8 1-92 mutant in differential detergent-permeabilized BY-2 cells. Representative micrographs of BY-2 cells either transiently transformed with N- or C-terminal-appended Myc-tagged-versions of tung CBR (A), non-transformed (B) or transiently (co-)transformed with Myc-GPAT8 1-92 expressed on its own or co-expressed with full-length HA-DGAT2 (C). Cells were fixed in formaldehyde at approximately 4 h after biolistic bombardment, permeabilized using either digitonin, which selectively permeabilizes the plasma membrane or Triton-X-100, which permeabilizes all cellular membranes (58), and then processed for (immuno)epifluorescence microscopy. Each micrograph is labeled at the top left with the name of either the (co-)expressed epitope-tagged protein or the corresponding endogenous marker protein (i.e. ER-lumenal calreticulin or cytosolic α-tubulin), as well as the detergent (Triton-X-100 or digitonin) used to permeabilize these cells. Also shown for each set of immunostained cells is the corresponding differential interference contrast (DIC) image. Note in (C) that Myc-GPAT8 1-92 either expressed on its own and localized to the cytosol (left three panels) or co-expressed with HA-DGAT2 and localized to ER subdomains (right three panels) was immunodetectable, whereas endogenous calreticulin in the same digitonin-permeabilized cells was not. Note also in (C) that the immunostaining attributable to co-expressed HA-DGAT2 in ER subdomains is not shown. Bar = 10 µm.

Table S1: List of synthetic oligonucleotide primers used in the isolation of tung *GPAT* genes and the construction of plasmids (see *Materials and Methods*; 98, 99)

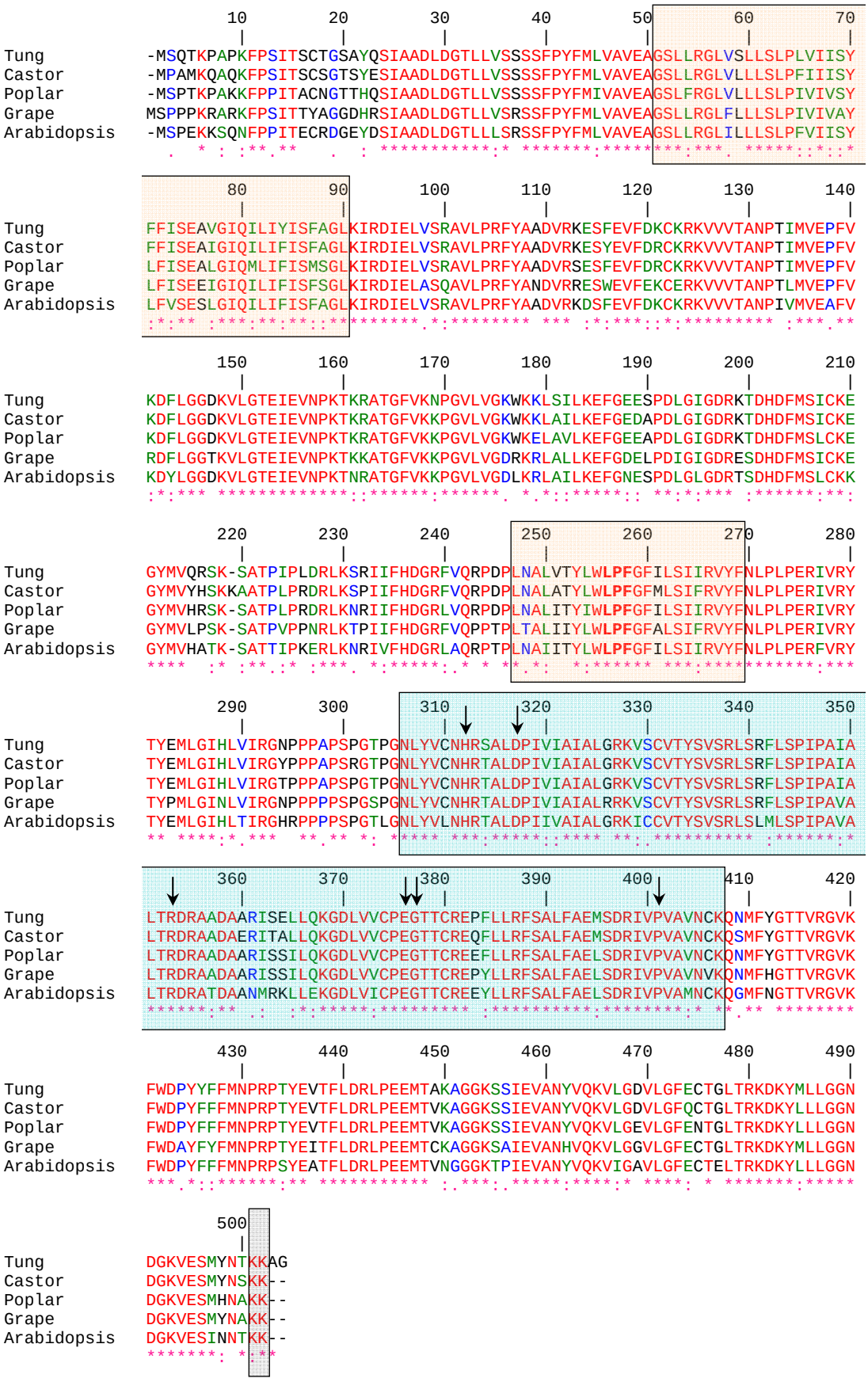

Figure S1

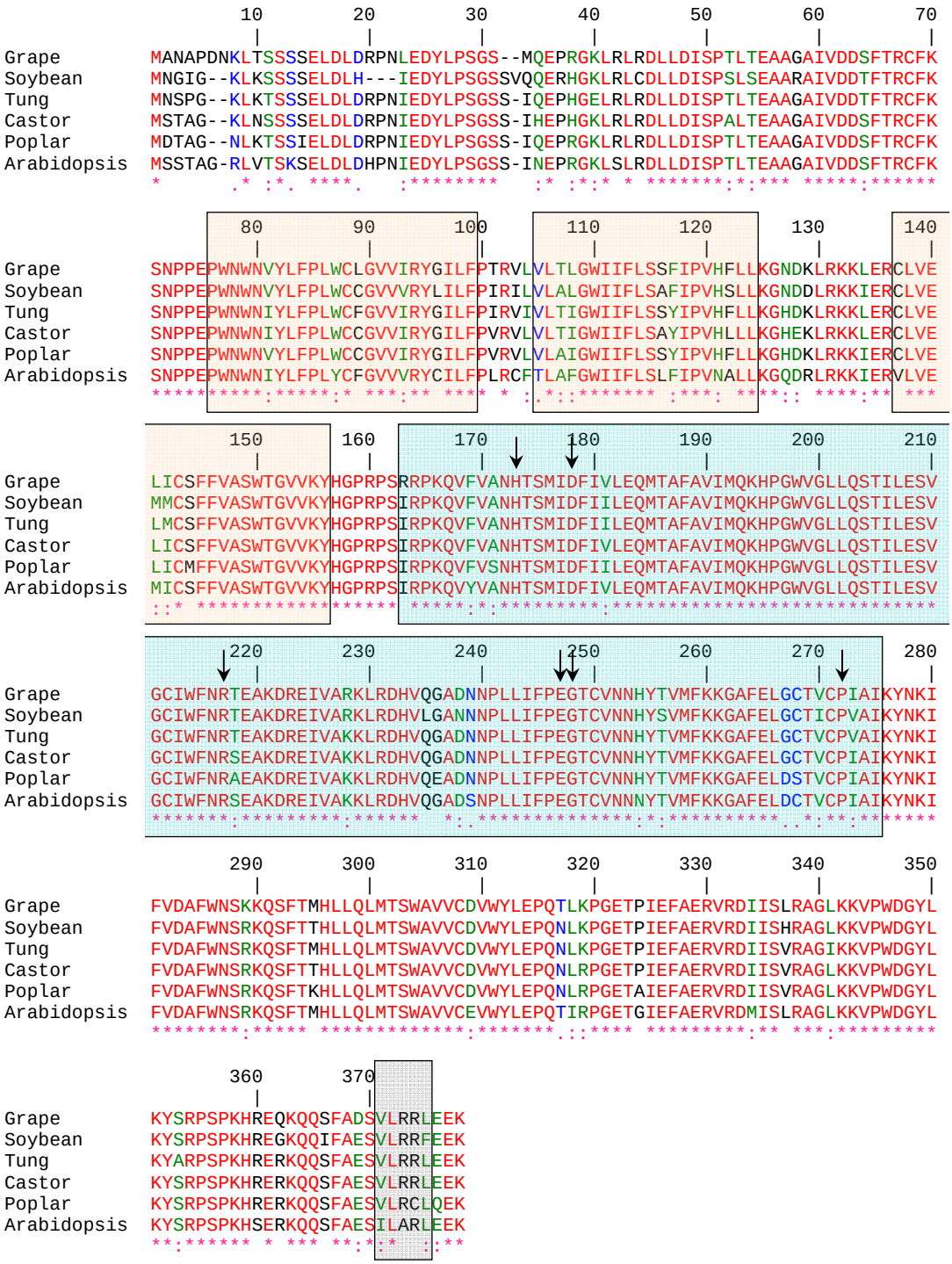

Figure S2

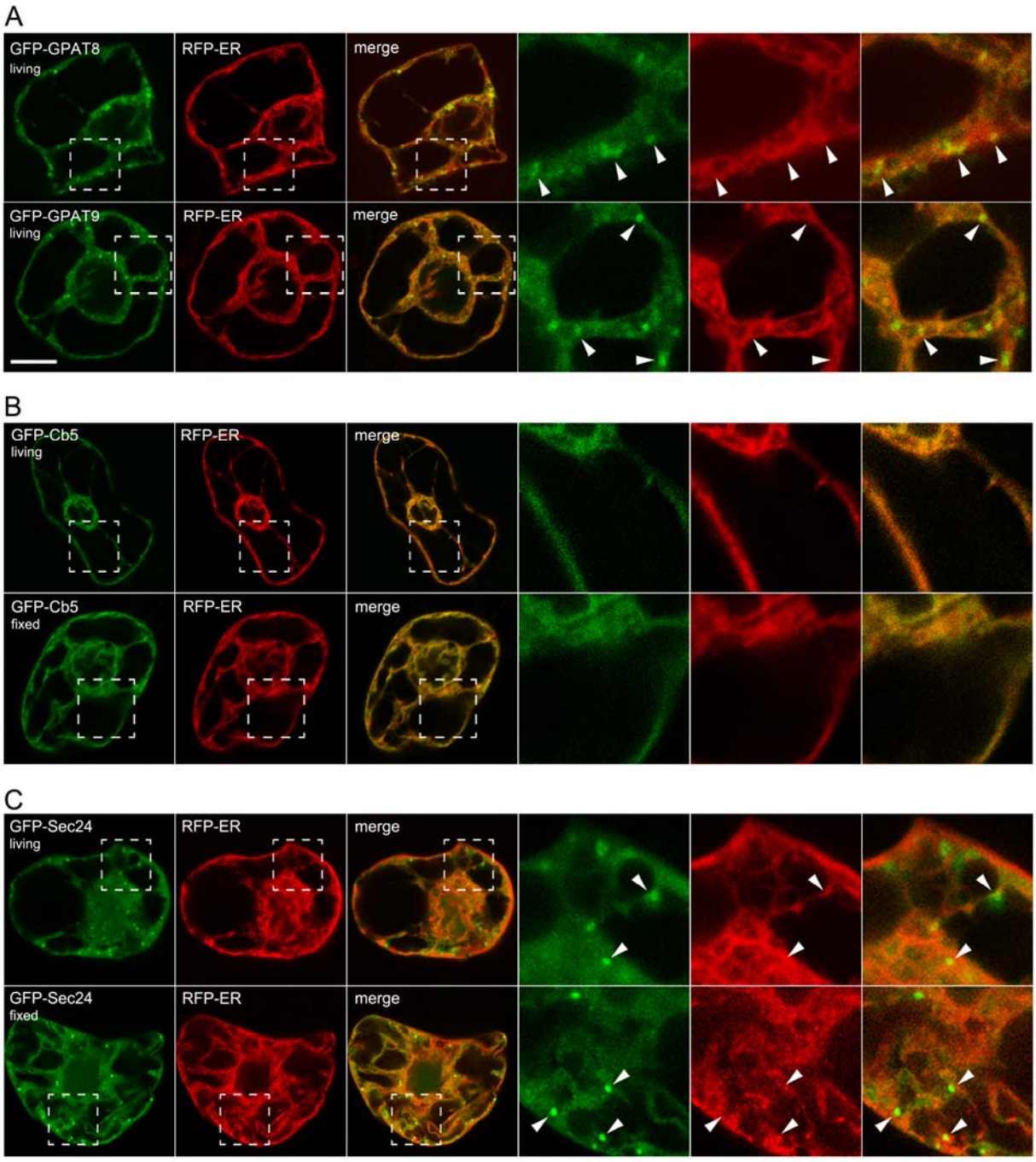
A
GFP-GPAT8
living
RFP-ER
merge
GFP-GPAT9
living
RFP-ER
merge
B
GFP-Cb5
living
RFP-ER
merge
GFP-Cb5
fixed
RFP-ER
merge
C
GFP-Sec24
living
RFP-ER
merge
GFP-Sec24
fixed
RFP-ER
merge

Figure S3

A

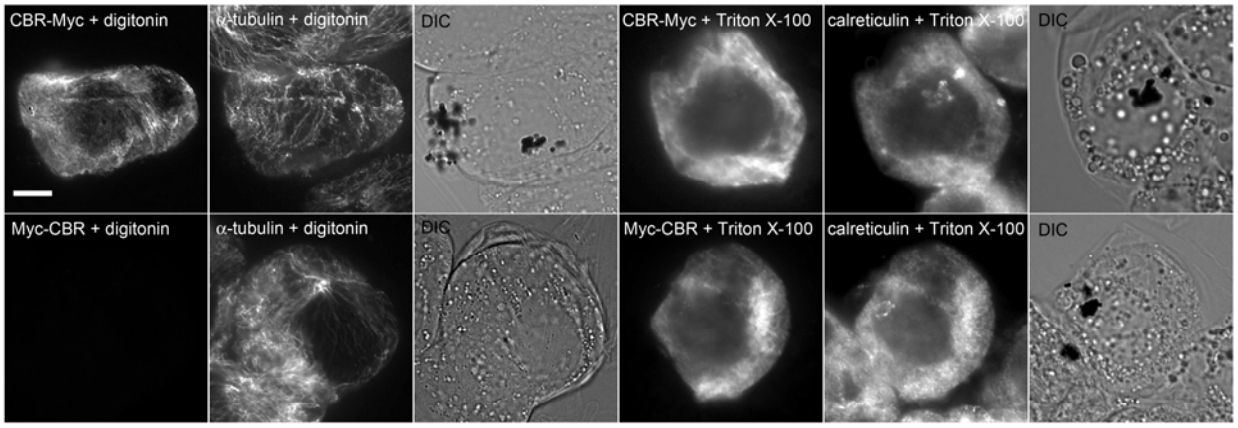

B

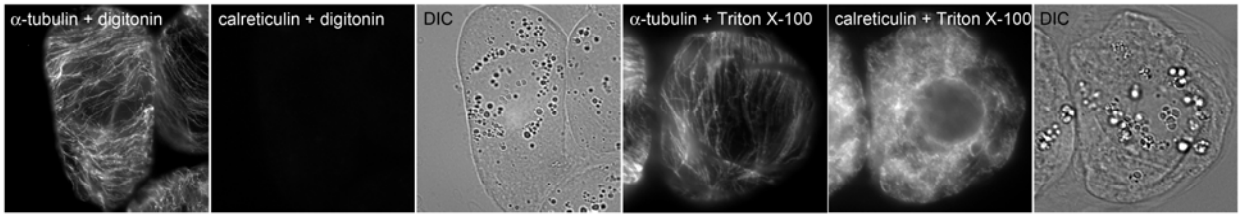

C

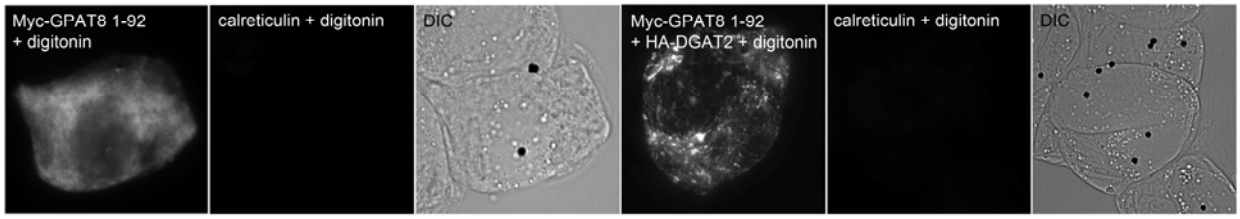

Figure S4